



HAL
open science

Unimolecular decomposition of methyl ketene and its dimer in the gas phase: theory and experiment

Imene Derbali, Helgi Rafn Hrodmarsson, Martin Schwell, Y Benilan, Lionel Poisson, Majdi Hochlaf, Mohammad Esmail Alikhani, J.-C. Guillemin, Emilie-Laure Zins

► **To cite this version:**

Imene Derbali, Helgi Rafn Hrodmarsson, Martin Schwell, Y Benilan, Lionel Poisson, et al.. Unimolecular decomposition of methyl ketene and its dimer in the gas phase: theory and experiment. *Physical Chemistry Chemical Physics*, 2020, 22 (36), pp.20394-20408. 10.1039/d0cp03921g . hal-02959792

HAL Id: hal-02959792

<https://hal.science/hal-02959792>

Submitted on 17 Nov 2020

HAL is a multi-disciplinary open access archive for the deposit and dissemination of scientific research documents, whether they are published or not. The documents may come from teaching and research institutions in France or abroad, or from public or private research centers.

L'archive ouverte pluridisciplinaire **HAL**, est destinée au dépôt et à la diffusion de documents scientifiques de niveau recherche, publiés ou non, émanant des établissements d'enseignement et de recherche français ou étrangers, des laboratoires publics ou privés.

Unimolecular Decomposition of Methyl Ketene and its Dimer in the Gas Phase: Theory and Experiment

Imene Derbali¹, Helgi Rafn Hrodmarsson*^{2,3}, Martin Schwell⁴, Yves Bénilan⁴, Lionel Poisson⁵, Majdi Hochlaf*⁶, Mohammad Esmail Alikhani¹, Jean-Claude Guillemin⁷,
Emilie-Laure Zins¹

¹*MONARIS UMR 8233 CNRS, Sorbonne Université, 4 place Jussieu, 75252 Paris Cedex 5,
France*

²*Synchrotron SOLEIL, L'Orme des Merisiers, St Aubin, BP 48, Gif sur Yvette, France*

³*Laboratory for Astrophysics, Leiden Observatory, Leiden University, PO Box 9513, NL-2300
RA Leiden, the Netherlands*

⁴*LISA UMR CNRS 7583, Université Paris Est Créteil and Université Diderot, Institut Pierre
Simon Laplace, 61 Avenue du Général de Gaulle, 94010 Créteil, France*

⁵*Université Paris-Saclay, CEA, CNRS, LIDYL, 91191 Gif-sur-Yvette, France*

⁶*Université Gustave Eiffel, COSYS/LISIS, 5 Bd Descartes 77454, Champs sur Marne, France*

⁷*Univ Rennes, École Nationale Supérieure de Chimie de Rennes, CNRS, ISCR-UMR6226, F-
35000 Rennes, France*

Total number of pages in manuscript: 33

Total number of pages in supporting information: 13

Tables: 5+6

Figures: 11+5

* Authors for correspondence:

Helgi Rafn Hrodmarsson: Phone: +31 629 413 569; E-mail 1: hr.hrodmarsson@gmail.com; E-mail 2 :
hrodmarsson@strw.leidenuniv.nl

Majdi Hochlaf: Email: hochlaf@univ-mlv.fr

34 Abstract

35 *We present a combined theoretical and experimental investigation on the single photoionization*
36 *and unimolecular photodissociation of gas-phase methyl ketene (MKE) and its neutral dimer*
37 *(MKE₂). The performed experiments entail the recording of photoelectron photoion*
38 *coincidence (PEPICO) spectra and slow photoelectron spectra (SPES) in the energy regime*
39 *8.7 – 15.5 eV using linearly polarized synchrotron radiation. We observe both dimerization and*
40 *trimerization of the monomer which brings about significantly complex and abstruse*
41 *dissociative ionization patterns. These require the implementation of theoretical calculations*
42 *to explore the potential energy surfaces of the monomer and dimer's neutral and ionized*
43 *geometries. To this end, explicitly correlated quantum chemical methodologies involving the*
44 *coupled cluster with single, double and perturbative triple excitations (R)CCSD(T)-F12*
45 *method, are utilized. An improvement in the adiabatic ionization energy of MKE is presented*
46 *(AIE = 8.937 ± 0.020 eV) as well as appearance energies for multiple fragments formed*
47 *through dissociative ionization of either the MKE monomer or dimer. In this regard, the synergy*
48 *of experiment and theory is crucial to interpreting the obtained results. We discuss the potential*
49 *astrochemical implications of this work in context of recent advances in the field of*
50 *astrochemistry and speculate on the potential presence and eventual fate of interstellar MKE*
51 *molecules.*

52 1. INTRODUCTION

53 A key question in astrophysics, astrochemistry, and astrobiology concerns the origins of
54 molecular complexity in space.¹⁻³ At the time of writing, well over 200 molecules have been
55 detected in the interstellar medium (ISM); approximately one third of them being complex
56 organics molecules (COMs) containing six atoms or more.⁴ COMs have been shown to
57 effectively form upon VUV photoprocessing of simple interstellar ice analogs⁵⁻⁸ but to explain
58 their abundance in the gas phase in cold molecular clouds requires a VUV- (or cosmic ray)
59 driven photodesorption paradigm to complement thermal desorption.¹ Ultracold gas phase
60 reaction kinetics measurements have, however, shown that chemical kinetics display
61 significantly anti-Arrhenius kinetics at temperatures approaching that of the interstellar medium
62 (ISM).^{9,10} The recent detection of cyanobenzene in the TMC-1 molecular cloud,¹¹ and the
63 assignment of several of the diffuse interstellar bands (DIBs) to transitions within the C_{60}^+
64 Buckyball cation,¹² have now challenged our basic notions of molecular complexity in space
65 and the upper limits to interstellar molecular complexity are quickly extending.

66 A significant portion of the COMs that have been detected in space are linear rigid
67 carbon chains. These may include nitrogen (such as cyanopolyynes¹³) and oxygen (such as the
68 HC_7O radical¹⁴ and ketene; $H_2C=C=O$ ¹⁵). A clear understanding of the VUV photodynamics
69 (including that of photoionization and photofragmentation) of these species and their
70 derivatives is crucial for further interpretation of astronomical data and the modelling of the
71 chemistry of interstellar media.

72 Methyl ketene ($H_3C-CH=C=O$; 1-Propen-1-one), called MKE in the following, is a
73 carbon chain molecule comprising a rigid CCO frame which is of astronomical interest, and
74 whose VUV laboratory data is scarce.¹⁶ Other prior work pertaining to MKE include e.g.
75 potential energy surface calculations¹⁷ and characterization of its infrared bands.¹⁸ Recently,
76 Bermúdez *et al.*¹⁹ recorded its mm-wave spectrum in the 50-330 GHz range, and those spectra
77 were used to search for MKE in various interstellar molecular inventories such as Sagittarius
78 B2 and TMC-1 in the Taurus Molecular Cloud, but unsuccessfully. Astronomically, MKE is
79 still expected to play a role as its isomer, propenal ($H_2C=CH-CHO$), which is merely 2.8 kJ/mol
80 more stable than MKE according to theory,¹⁹ has been tentatively detected in Sagittarius B2.²⁰
81 In order to further contextualize this current non-detection of MKE, particularly in the light of
82 its homolog ketene ($H_2C=C=O$) having been detected in the 1970's,¹⁵ its VUV photodynamics
83 are of great relevance.

84 Further indications of the astronomical relevance of MKE have been found in laboratory
85 ice chemistry. MKE has been formed in certain interstellar ice analogues which were inspected

86 in order to find a potential link to the formation of propylene oxide, the first chiral molecule to
87 be detected in the ISM.²⁰ A potential paradigm of MKE's chemical evolution could involve
88 formation on icy grains and subsequently undergo further chemical reactions, and/or thermal,
89 chemical, or photo-induced desorption. The recent detection of propylene oxide makes a strong
90 case for the detection of MKE as both species can form in such icy grains. A problem with the
91 determination of MKE formation in ices is that the ν_4 fundamental band of MKE overlaps with
92 the infrared stretching vibration of CO. Hence, threshold photoelectron spectroscopy has been
93 suggested as a desirable method to determine the formation of MKE in ices.²¹ A similar
94 methodology has been applied to infer the formation of MKE in the reaction between the
95 methyldene radical and acetaldehyde using a multiplexed photoionization mass spectrometer²²
96 but using a previously recorded photoelectron spectrum of MKE¹⁶ to identify it as a product in
97 the reaction.

98 Here we present a combined experimental and theoretical study of the photoionization
99 and photofragmentation dynamics of MKE and its dimer, including their threshold
100 photoionization spectra. This continues ongoing work of dedicated and synergistic
101 experimental and theoretical characterizations of astrochemically / astrobiologically relevant
102 molecules.²³⁻²⁹ Our results are discussed in context of modern advances in experimental
103 astrochemistry and the potential presence of gaseous MKE in space.

104

105 **2. METHODS**

106 **2.1. Experimental**

107 Experiments were performed at the DESIRS VUV beamline at the SOLEIL synchrotron in
108 Saint-Aubin, France.³⁰ Horizontally polarized radiation in the 8.7-15.5 eV range was generated
109 by an undulator³¹ and passed through a gas filter filled with Argon to suppress higher harmonics
110 from the undulator by four to five orders of magnitude. The photon beam was dispersed by a
111 6.65 m normal incidence monochromator with 200 grooves/mm grating. The photon flux of the
112 resulting beam was between 10^{12} and 10^{13} photons/sec and was directed into the beamline
113 endstation where the SAPHIRS chamber is located.³² It contains the DELICIOUS III double-
114 imaging photoion photoelectron coincidence (*i*²PEPICO) spectrometer³³ in which the
115 synchrotron radiation was interfaced with a molecular beam under a right angle. The generated
116 photoelectrons and photoions are accelerated in opposite directions with a DC electric field of
117 1000 V. The electron side contains a velocity map imaging spectrometer and the ion side a
118 modified Wiley McLaren time-of-flight 3D momentum imaging spectrometer. This setup

119 allows a PEPICO scheme to be employed, mass-tagging the recorded electron images and
120 eliminating any spurious background compounds.

121 MKE was produced by pyrolysis at 600°C under 0.1 mbar of the commercially available
122 propionic anhydride. The by-product propanoic acid was removed by selective condensation in
123 a first U-tube immersed in a cold bath at -70 ° C while the formed MKE was trapped in a second
124 U-tube immersed in a 77 K bath. This trap was then fitted on the spectrometer and allowed to
125 warm to -120°C by immersion in a cooled isopentane bath.

126 It is thus easily vaporized into a He gas stream that flows through the first gas nozzle
127 inside the differentially pumped SAPHIRS jet chamber, using a backing pressure of
128 approximately 500 mbar. This gas flow is then streamed through a second 50 μm pinhole nozzle
129 leading to the ionization chamber. The applied electric field in the ionization source of
130 DELICIOUS III induces a Stark effect which effectively decreases the ionization energies of
131 the compounds entering the chamber. The Stark effect is approximately 23.5 meV and is
132 corrected for in the energy calibration which uses the signals of ionized background O₂.
133 Intensity calibrations were performed using the recorded flux over the appropriate energy range
134 which has been measured with an AXUV100, IRD Si photodiode. Image inversions are
135 performed with the pBASEX algorithm.³⁴

136 To obtain the threshold photoelectron spectrum we employed the slow photoelectron
137 spectroscopic method (SPES) which has been detailed previously.³⁵ In brief, following the
138 inversion of mass-tagged images recorded with DELICIOUS III, the ionization intensities can
139 be plotted in matrix form as a function of the electron kinetic energy (*eKE*) and the photon
140 energy. This two-dimension photoelectron spectral matrix (2D-PES matrix) contains a wealth
141 of spectroscopic information and by investigating different “cuts” through the matrix,
142 properties such as photon-dependent electron kinetic energy distributions, partial
143 photoionization cross sections, etc. can be obtained.³⁶ The recorded 2D-PES matrix of MKE
144 (*m/z* 56) is presented in Figure S1 in the SI.

145 To extract the SPES from the 2D-PES matrix, the pixel intensities are diagonally
146 integrated along the electron signals from *eKE* = 0 up to an arbitrary value, *eKE*_{max}, carefully
147 chosen to find a compromise between signal intensity and energy resolution. The total energy
148 resolution is a convolution of the photon resolution and the electron bandwidth. Typical energy
149 resolutions are approximately 20 meV for *eKE*_{max} ranging between 50 and 100 meV.³⁷

150

151 2.2. Theoretical

152 We performed the geometry optimizations (opt), in the C1 point group, of neutral and cationic
153 MKE and of its neutral and ionized dimer using the PBE0 density functional,³⁸ where the atoms
154 are described by the augmented correlation-consistent aug-cc-pVTZ (aVTZ) basis sets of
155 Dunning and co-workers.^{39,40} Subsequently, we computed the harmonic to assess the minimal
156 nature of the optimized stationary point (all positive frequencies) and on top of that, we deduced
157 their anharmonic frequencies using the second-order vibrational perturbation theory (VPT2)
158 approach.^{41,42} These electronic structure computations were done using GAUSSIAN 09
159 Revision E.⁴³ The standard options as implemented in this suite of programs were adopted. The
160 GAUSSIAN package was also used to generate the photoelectron spectrum of MKE via the
161 derivation of the Franck Condon (FC) factors for the MKE (X) \rightarrow MKE⁺ (X) ionization
162 transition.^{44,45} Indeed, the FC analysis was done by means of the time-independent adiabatic
163 Hessian Franck-Condon (TI-AH|FC) model.⁴⁶⁻⁴⁹ The stick simulated vibrationally resolved
164 electronic spectrum was later convolved with a 20 meV bandwidth Gaussian profile,
165 corresponding to the present experimental resolution.

166 These density functional theory results were used as starting points for full re-
167 optimization of the neutral and cationic MKE and of the cationic fragments using the explicitly
168 correlated coupled cluster with single, double and perturbative triple excitations (R)CCSD(T)-
169 F12 method,⁵⁰⁻⁵⁴ and implemented in the MOLPRO package.⁵⁵ The atoms were described by
170 the augmented correlation-consistent cc-pVTZ-F12 basis set.⁵⁶ Then, single point (SP)
171 computations were done for the inclusion of core-valence (CV),⁵⁷ and scalar relativistic⁵⁸
172 effects at the (R)CCSD(T)/cc-pwCVTZ⁵⁹ and (R)CCSD(T)/cc-pVTZ-DK,^{58,60,61} respectively,
173 using the composite scheme detailed in our previous works.²⁷ **The accuracy of this composite**
174 **theoretical approach was estimated to be $\pm 10-20$ meV.**²⁵ For the MKE dimer, the CV and SR
175 corrections are done on top of the PBE0/aVTZ computations. Although less accurate than the
176 (R)CCSD(T)-F12 based composite scheme computations, the PBE0/aVTZ//+CV+SR
177 methodology is accurate enough for the interpretation of the experimental features measured
178 here.⁶² **Furthermore, it was checked that the wB97XD functional leads to similar results from a**
179 **geometrical and energetical point of view. Table S1 and S2 allow comparison between the**
180 **geometry and energetics obtained using these two functionals in combination with the aug-cc-**
181 **pVTZ basis set.** For the derivation of the adiabatic ionization energies (AIE) and appearance
182 energies (AE), we refer to our recent results pertaining to propynal.²⁷ **It is worth mentioning**
183 **that a barrier could be associated to some of the considered fragmentations channels. However,**
184 **the agreement between the experimental appearance energies and the calculated ones without**

185 considering any barrier suggest that all the considered mechanisms are barrierless, concerted
 186 mechanisms.

187

188 3. RESULTS & DISCUSSION

189 Here, we present the combined experimental and theoretical results pertaining to the single
 190 photon ionization of MKE and its dimer in the gas-phase from the ionization threshold to
 191 15.5 eV. It is well documented that organic molecules can easily form clusters in supersonic
 192 expansions,⁶³ and this is indeed the case here for MKE. As will be shown, the experiment and
 193 theory complement one another well to shed light on the complications associated with the
 194 effects of dissociative ionization following the clustering of MKE monomers.

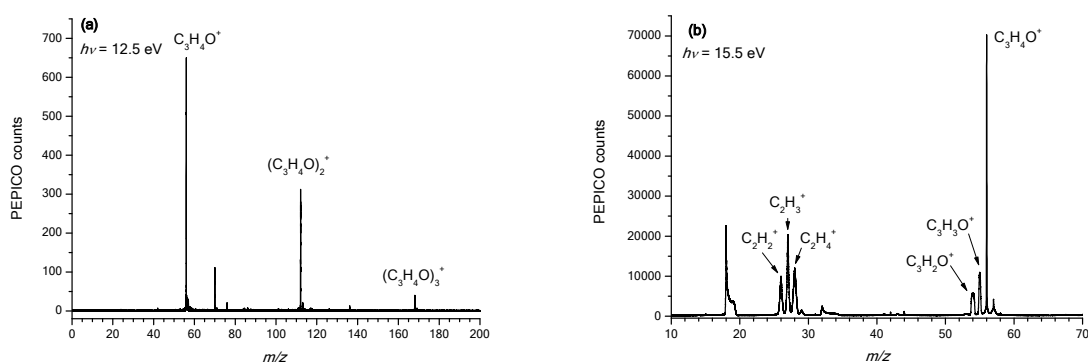
195

196 3.1 Time-of-flight mass spectra (TOF-MS)

197 Time-of-flight mass spectra (TOF-MS) recorded at photon energies of 12.5 and 15.5 eV are
 198 presented in Figure 1. At 12.5 eV the monomer, the dimer, and the trimer are clearly visible in
 199 descending order of intensity at m/z 56, m/z 112, and m/z 168, respectively (Fig. 1a). Larger
 200 clusters are not observed. A signal at m/z 70 is visible as well, corresponding to residual signals
 201 of 2-aminoproprionitrile that were used in a prior experiment and whose results are subject to
 202 another publication. A weaker residual signal at m/z 76 is observed as well but the identity of
 203 its carrier is unclear. It is possible that it is an impurity from the thermal degradation of
 204 propionic anhydride, with the elemental formula $C_3O_2H_8$ (in which case it could be an isomer
 205 of propanediol) or $C_2O_3H_2$ (in which case it could be 1,2,4-trioxolane or hydroxyacetic acid).

206

207



208

209 **Figure 1.** Time-of-flight mass spectrum (TOF-MS): (a) of MKE, its dimer, and its trimer,
 210 photoionized at $h\nu = 12.5$ eV and (b) of MKE and the different fragments formed by
 211 photoionization at $h\nu = 15.5$ eV.

212

213 At 15.5 eV, the dimer and trimer signals are not visible but several masses lighter than
214 the monomer appear in the TOF-MS (Fig. 1b). Here, the parent ion is still the most intense mass
215 peak. The lighter masses include m/z 55 and 54 with low intensity and correspond to the
216 fragment ions resulting from the loss of atomic and molecular hydrogen to yield $C_3H_3O^+$ and
217 $C_3H_2O^+$, respectively. Other notable fragment signals include $C_2H_4^+$ (m/z 28), $C_2H_3^+$ (m/z 27),
218 and $C_2H_2^+$ (m/z 26). The m/z 57 mass peak corresponds to a mixture of the monomer's ^{13}C
219 isotopomer and the protonated monomer (to be discussed below). Finally, background signals
220 are observed due to ionized residual water (m/z 18) and molecular oxygen (m/z 32) in the
221 ionization chamber. We note that autoionization bands of O_2 were used to calibrate the energy
222 scale of the scan used to record the SPES between 7.8 and 12.5 eV.

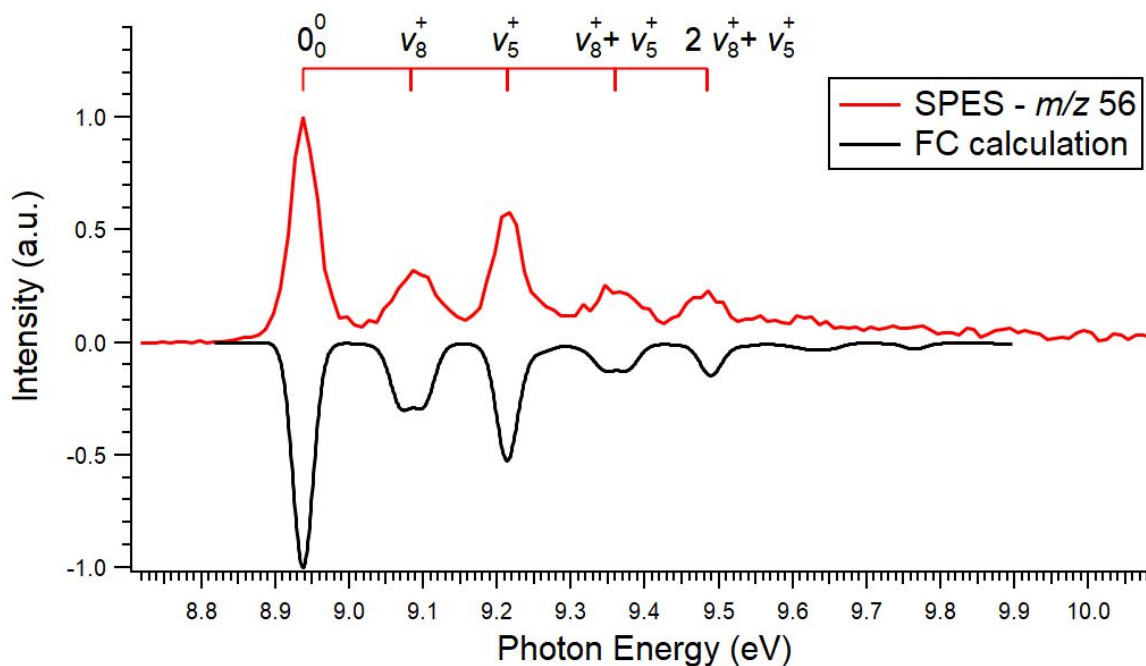
223

224 3.2 SPES of the MKE monomer

225 3.2.1 Ground state

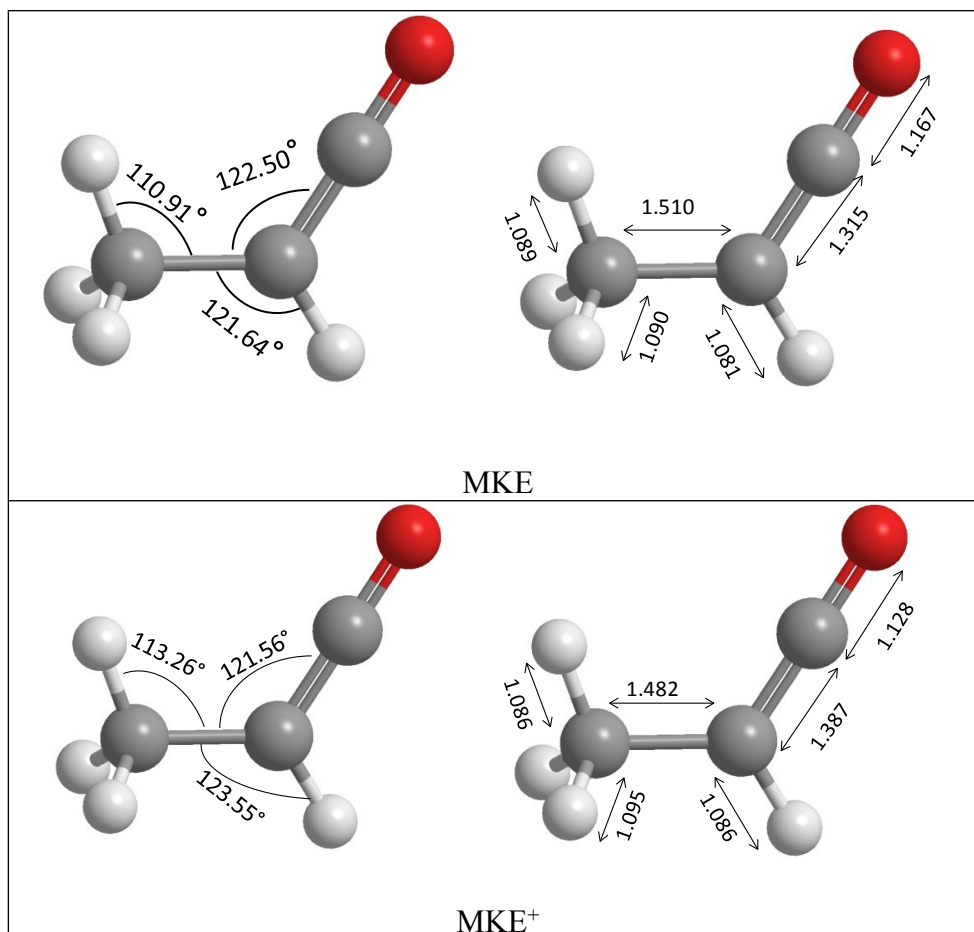
226 Figure 2 presents the slow photoelectron spectrum (SPES) of the parent ion (m/z 56). The SPES
227 includes a vibrational progression corresponding to the population of the ground electronic state
228 of MKE. The full assignment of the ground state vibrational progression is discussed here
229 below.

230 The adiabatic ionization energy (AIE) of MKE can be measured from the SPES as the
231 center of the first and most intense band. Here, we deduce a value of $AIE_{\text{exp}} = 8.937 \pm 0.020$ eV.
232 To verify this value, we also performed a theoretical calculation of AIE at the (R)CCSD(T)-
233 F12/cc-pVTZ-F12(opt) (+CV+SR+ZPVE) (SP) level and obtained a value of $AIE_{\text{calc}} =$
234 8.917 eV, in good agreement with the experiment. Further details of the calculation, notably
235 geometries of involved neutrals and cations, are presented in Tables S3, S4 and S5 of the SI.
236 The calculated AIE of MKE is also in agreement with prior VUV photoionization experiments
237 by Bock *et al.* who found a value of 8.95 eV for the adiabatic ionization energy (no precision
238 is given in this earlier work).¹⁶ In this regard, our measurements present an improvement in
239 accuracy.



240
 241 **Figure 2.** Experimental (red) and theoretical (black) SPES of the MKE parent ion (m/z 56). The
 242 SPES is obtained by using $eKE_{\max} = 100$ meV when diagonally projecting the 2D-PES matrix.
 243 The experimental adiabatic ionization energy (AIE) is taken as the median of the 0_0^0 band which
 244 is located at 8.937 eV. The assignment of the vibrational progression is discussed in the text.
 245 The calculated curve has been shifted upwards in energy by 20 meV to coincide with the
 246 experimental results.

247 In their electronic ground states, both neutral MKE and its cation (Figure 3) belong to
 248 the C_s symmetry point group. For neutral MKE, our computed geometry is close to the one
 249 calculated earlier by Bak *et al.*⁶⁴ Closer inspection of the ionic and neutral equilibrium
 250 geometries reveals a subtle geometrical deformation upon ionization, where the C=O double
 251 bond and the C-C single bond slightly contract while the C=C double bond extends.
 252 Furthermore, the HCC bond angle of the methyl group changes from 110.91° to 113.26° . These
 253 small changes are at the origin of the short vibrational progression in the ground state of MKE^+ .
 254 Therefore, the general appearance of the SPES spectrum of Figure 2 can be attributed to the
 255 similarities of the equilibrium geometries of the neutral and cationic forms of MKE. Indeed, a
 256 short vibrational progression is expected upon ionization of the monomer, in accordance with
 257 the FC principle. The recorded SPES typifies this expectation.



258 **Figure 3.** Main geometrical parameters of the ground of neutral MKE and its cation. Distances
 259 are given in Å (right panels) and angles are given in degrees (left panels). These geometries are
 260 computed at the (R)CCSD(T)-F12 / cc-pVTZ-F12 level.

261
 262 The assignment of the monomer's SPES is made possible with quantum chemical
 263 calculations. It is guided by the anharmonic wavenumbers calculated for the MKE⁺ ground state
 264 at the PBE0/aug-cc-pVTZ level of theory. Table 1 presents the anharmonic wavenumbers of
 265 the eighteen normal modes of vibration arranged in descending order under *a'* and *a''* symmetry
 266 species. The energies of the observed band maxima in our experiment and comparison with
 267 theory are presented in Table 2. Experimental transition energies are also marked by vertical
 268 bars in Figure 2. Below 10 eV these bands are assigned to the photoionization transitions
 269 populating the MKE⁺ ground state vibrational levels.

270 The first and most intense band is assigned to the transition of neutral ground state MKE
 271 to the ground state of the MKE⁺ cation. For the lower intensity band at 9.083 eV ($\nu_{exp}^+ = 1177.6$
 272 cm^{-1}) we propose that it corresponds to the C-C stretching mode between the methyl C-atom
 273 and the terminal ketene C-atom. This value is in excellent agreement with the computed value
 274 ($\nu_8^+ = 1159.3 \text{ cm}^{-1}$).

275 **Table 1.** Anharmonic wavenumbers (E_{anhar} , cm^{-1} and eV) of the fundamental bands of the
 276 ground state of MKE^+ as computed at the PBE0/aug-cc-pVDZ level of theory. We also give
 277 their assignment.

Vibrational Mode	Sym.	E_{anhar}		Assignment
		cm^{-1}	eV	
ν_1^+	a'	3181.4	0.394	CH (sp^3) stretching
ν_2^+	a'	3155.9	0.391	CH (sp^2) stretching
ν_3^+	a'	3039.3	0.377	CH (sp^3) stretching
ν_4^+	a'	2996.6	0.372	CH_3 sym. stretching
ν_5^+	a'	2298.1	0.285	C=O stretching
ν_6^+	a'	1470.7	0.182	CH (sp^3) in-plane-bending
ν_7^+	a'	1376.3	0.171	C-C stretching
ν_8^+	a'	1159.3	0.144	C-C stretching
ν_9^+	a'	1097.6	0.136	CH_3 (sp^3) asym. stretching
ν_{10}^+	a'	856.1	0.106	CH (sp^3) bending
ν_{11}^+	a'	621.6	0.077	C-C=C in-plane-bending
ν_{12}^+	a'	206.7	0.026	C=C=O in-plane-bending
ν_{13}^+	a''	1408.9	0.175	CH (sp^3) rocking
ν_{14}^+	a''	1309.8	0.162	CH (sp^2) in-plane-bending
ν_{15}^+	a''	931.9	0.116	CH_3 wagging
ν_{16}^+	a''	667.8	0.083	CH (sp^2) out-of-plane-bending
ν_{17}^+	a''	451.4	0.056	C=C=O out-of-plane-bending
ν_{18}^+	a''	119.3	0.015	CH_3 torsion

278

279 **Table 2.** Tentative assignment of the observed vibrational progression resolved in the SPES of
 280 the monomer in the 8.7-9.5 eV photon energy range (Figure 2).

Band position [eV]	Experiment [cm^{-1}]	Theory [cm^{-1}]	Assignment
8.937	0.0 ^a	0.0 ^a	Adiabatic IE, 0_0^0
9.083	1177.6	1159.3	ν_8^+
9.214	2234.1	2298.1	ν_5^+
9.360	3411.7	3457.4	$\nu_8^+ + \nu_5^+$
9.484	4411.8	4616.7 / 4596.2 / 4555.0	$2\nu_8^+ + \nu_5^+ / 2\nu_5^+ /$ $\nu_9^+ + \nu_8^+ + \nu_5^+$

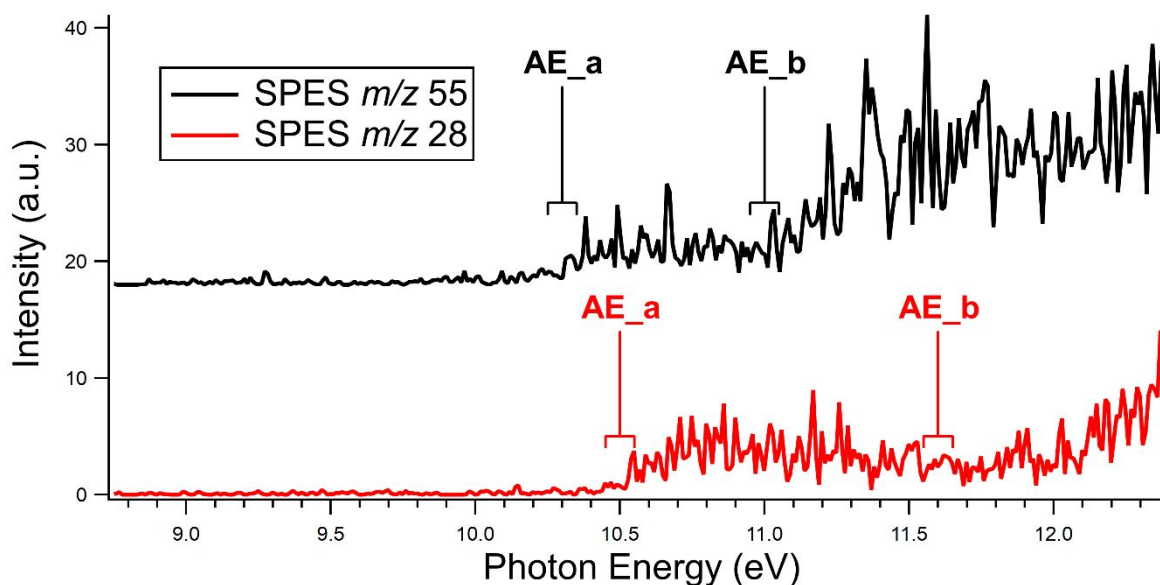
281 ^aUsed as reference.

282 We propose that the next band in the SPES ($\nu_{exp}^+ = 2234.1 \text{ cm}^{-1}$) corresponds to the
 283 ν_5^+ stretching mode of C=O. The other bands in the SPES can then be tentatively assigned to
 284 combination modes of these two ($\nu_8^+ + \nu_5^+$) stretching modes. Comparison between
 285 experiment and theory is quite satisfactory (differences are within 50 cm^{-1}) except for the last
 286 band observed at 9.484 eV where it exceeds 200 cm^{-1} (or 25 meV). Therefore, we cannot
 287 exclude the possibility of **either an overtone of the ν_5^+ stretching mode or** a contribution from
 288 the ν_9 band (corresponding to the asymmetric C-H stretching vibration in the methyl group),
 289 resulting in the assignment, i.e. $\nu_9^+ + \nu_8^+ + \nu_5^+$.

290

291 3.2.2 Dissociative ionization of MKE

292 Figure 4 presents the SPES associated with the formation of two cations, namely $\text{C}_3\text{H}_3\text{O}^+$ (m/z
 293 55) and C_2H_4^+ (m/z 28) which start to appear at around 10 eV. The two fragment ions are also
 294 visible in the 15.5 eV TOF-MS presented in Figure 1b. Both signals are fairly weak and diffuse.
 295 Nevertheless, they allow us to measure dissociative ionization thresholds of MKE forming these
 296 ionic fragments, which are indicated in Fig. 4.



297

298 **Figure 4.** SPES of two fragments formed by dissociative photoionization of MKE. The m/z 55
 299 fragment ion is shown in black and corresponds to H-loss from the parent cation. The m/z 28
 300 fragment ion is shown in red and corresponds to CO loss from the parent cation. In both the m/z
 301 55 and m/z 28 SPES we observed respectively two appearance energies, AE_a and AE_b, for
 302 two fragments, a and b, having the same mass. The ranges of the four AEs are indicated as
 303 estimated by the experimental accuracy. See text for further details.

304 The m/z 55 SPES corresponds to the loss of an H-atom. From the theoretical calculations
 305 on ionization and fragmentation thresholds (see Table 3), it can be inferred that the H loss is
 306 from the methyl group since the experimental onset at $AE_b = 11.00 \pm 0.05$ eV corresponds
 307 fairly well to the calculated value of $AE_{calc} = 10.78$ eV. In the SPES of m/z 55 there seems to
 308 be some weak structure between 10.2 eV and 11.0 eV, with an onset energy of approximately
 309 10.2 eV (AE_a). As will be discussed below, this structure may arise from the dissociation of
 310 the ionized MKE dimer.

311 The m/z 28 SPES corresponds to the loss of neutral CO, as is inferred from the quantum
 312 chemical calculations (cf. Table 3). It shows two bands with origins at $AE_a = 10.50 \pm 0.05$ eV
 313 and $AE_b = 11.70 \pm 0.10$ eV (see Fig. 4). In this context, there are two isomers of $C_2H_4^+$ ions
 314 that can potentially be formed. The optimized structures of these two considered $C_2H_4^+$ ions are
 315 shown in Figure 5. The two experimental values of the fragment AEs we deduced from the
 316 SPES, AE_a and AE_b , are in excellent agreement with the theoretically calculated appearance
 317 energies of the two isomers shown in Figure 5 ($AE_{calc1} = 10.508$ eV and $AE_{calc2} = 11.585$ eV;
 318 cf. Table 3). We can therefore assign the observed m/z 28 thresholds to the formation of two
 319 different isomers of $C_2H_4^+$ by dissociative photoionization of MKE.

320

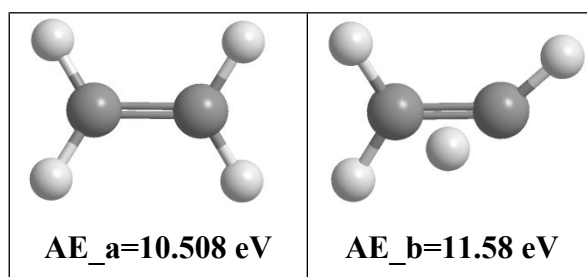
321

322

323

324

325



326 **Figure 5.** Optimized structures of two isomers of $C_2H_4^+$ calculated at the (R)CCSD(T)-F12 /
 327 cc-pVTZ-F12 level. Theoretical AEs are indicated. See text for more details.

328

329 In order to cover the entire dissociative photoionization potential energy surface of
 330 MKE^+ , several other fragmentation pathways were considered in the quantum-chemical
 331 calculations. They are presented in Figure 6. The respective calculated AEs are summarized in
 332 Table 3 together with some of the results of the calculations and the experimental AEs
 333 determined in this work.

334 Other weaker dissociation channels that may be relevant include the loss of molecular
 335 hydrogen, H_2 , to form the m/z 54 propadienone isomer ($H_2C=C=C=O^+$). While the m/z 54, 27,
 336 and 26 mass signals are too weak to obtain a viable SPES, we can attain an experimental value
 337 of the appearance energy by using the point where the ion signals exceed the background signals

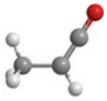
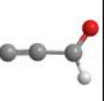
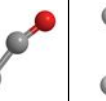
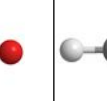
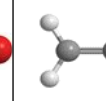
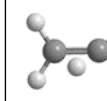
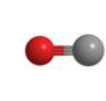
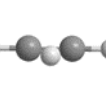
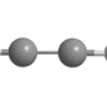
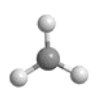
338 in their total ion yield curves obtained by accumulating signal at 15.5 eV (Figure S2 in the SI).
339 This method is less accurate than using the SPES but is nonetheless an acceptable form of
340 obtaining approximate fragment appearance energies.²⁵

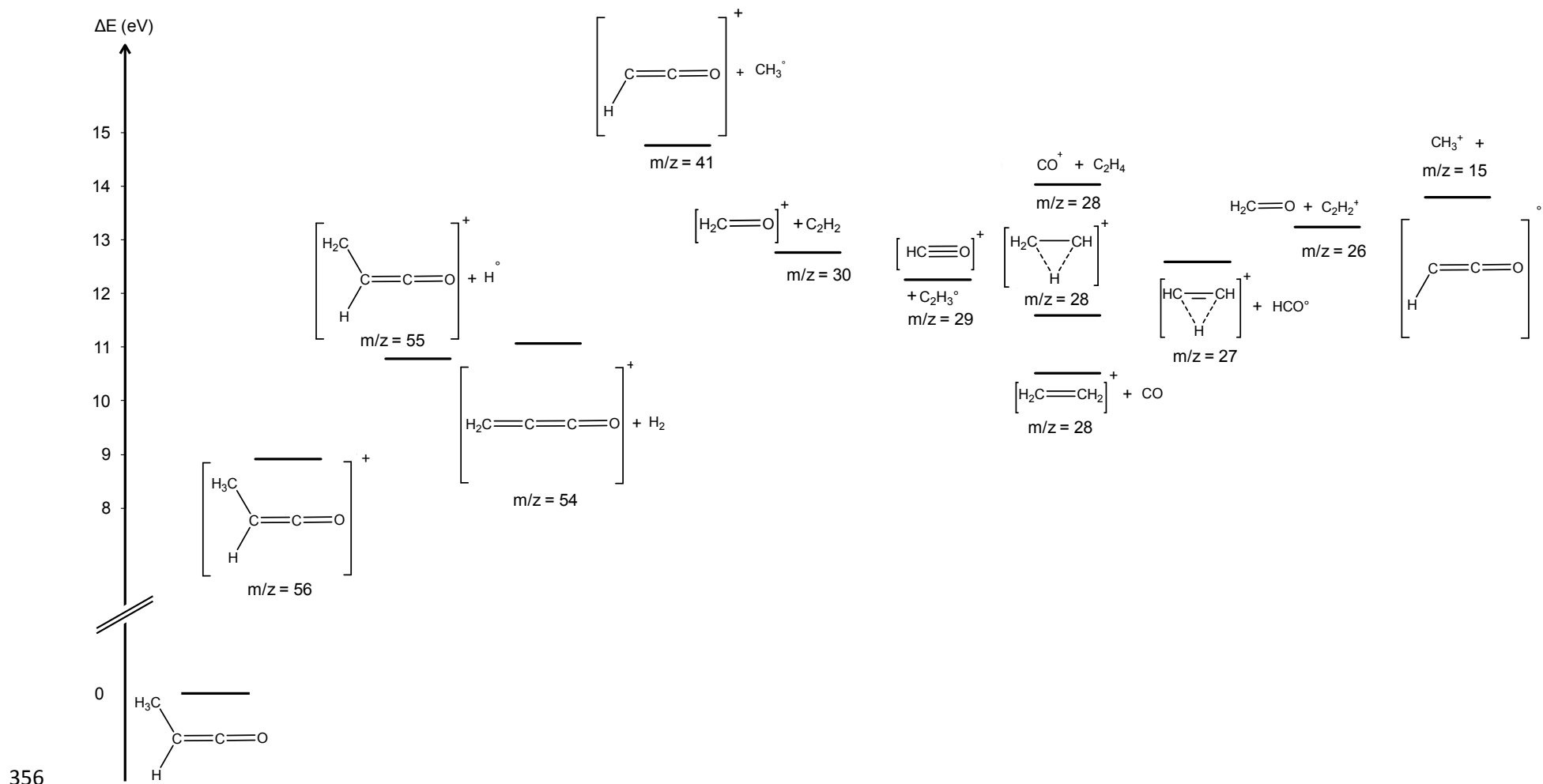
341 For the m/z 54 signal, there is a discrepancy between theory and experiment which lies
342 in the AE values. Indeed, the experimental AE value of this fragment from the monomer is 0.4
343 eV lower than the theoretically derived one. Since the accuracy of the theoretical methodologies
344 is better than 0.4 eV as established in our previous works, the question is raised whether the
345 fragment originates from the monomer at all or whether it originates from dissociative
346 photoionization of the MKE dimer or higher multimers. This is further detailed below.

347 For the m/z 27 and m/z 26 fragments, the agreement between experiment and theory is
348 worth mentioning though these discrepancies are somewhat smaller than that for the m/z 54
349 signal (0.1 eV and 0.25 eV, respectively). This could suggest a second mechanism in play in
350 which these fragments are formed by dissociative ionization of the dimer or higher multimers.
351 As with the m/z 54 signal, this is discussed below.

352 **Table 3.** Calculated and measured adiabatic ionization energies (AIEs) of MKE and the appearance energies (AEs) of the different fragmentation
 353 pathways of the resulting cation (in eV). The most stable structures which correspond to our experimental results are presented. Details of the
 354 computational results are given in Table S6 in the SI.

355

	Ionization	Fragments										
Formula	$C_3H_4O^+$	$C_3H_3O^+$	$C_3H_2O^+$	C_2HO^+	CH_2O^+	HCO^+	$C_2H_4^+$	$C_2H_4^+_{-1}$	CO^+	$C_2H_3^+$	$C_2H_2^+$	CH_3^+
Molecular structures												
		+ H	H ₂	CH ₃	C ₂ H ₂	C ₂ H ₃	+ CO	+ CO	C ₂ H ₄	H+CO	H ₂ +CO	C ₂ HO
												
m/z	56	55	54	41	30	29	28	28	28	27	26	15
AIE or AE Calc.	8.917	10.780	12.702	14.756	12.763	12.261	10.508	11.585	14.034	13.205	13.154	13.790
AIE or AE Exptl.	8.937 ± 0.020	11.00 ± 0.05	12.3 ± 0.1				10.50 ± 0.05	11.60 ± 0.05		13.1 ± 0.1	12.9 ± 0.1	



357 **Figure 6.** Dissociative ionization fragmentation pathways of the MKE cation considered in the quantum-chemical calculations and relative energies
 358 (ordinate) compared to the neutral MKE. The abscissa corresponds to descending m/z values of the formed cationic fragments.

3.3 Slow Photoelectron Spectrum (SPES) of the MKE dimer

3.3.1 Ground state

At higher m/z values in the 12.5 eV TOF-MS presented in Figure 1a, the MKE dimer and trimer (abbreviated MKE₂ and MKE₃) are observed. Here we present the recorded SPES of MKE₂ and discuss its dissociative ionization which affects the monomer signals at energies above the ground state as mentioned above.

To further understand the formation and structure of MKE₂, its structure was theoretically optimized at the PBE0/aVTZ level of theory (see Table S4 of the SI). Appearance energies of the fragments (C₃H₄O)·H⁺ (m/z 57) and (C₃H₅O)·H⁺ (m/z 58) are obtained indicating intramolecular H transfer. Indeed, the ionization process of the dimer is accompanied by such intramolecular isomerization and subsequent unimolecular fragmentation processes, as already demonstrated for other organic dimers.^{65–67}

Figure 7 displays the SPES corresponding to the photoionization of MKE₂ (m/z 112). The ionization processes remain mainly direct since the energy of the electron distribution rises correspondingly to the photon energy. The SPES comprises a single broad band extending from 8.75 to 9.60 eV where its intensity abruptly drops. The shape of the SPES curve reveals that the photoionization of the dimer results in a broad distribution due to unfavorable FC factors during the (C₃H₄O)₂ + $h\nu$ → (C₃H₄O)₂⁺ + e⁻ photoionization transition. This strongly suggests that the structure of the dimer is non-covalent in nature. We also note here that possible covalent dimers (for example 4-ethylidene-3-methyl-2-oxetanone) or other multimers, eventually present in the sample, would certainly possess a saturation vapor pressure that is too low at room temperature in order to be vaporized in our experimental conditions.

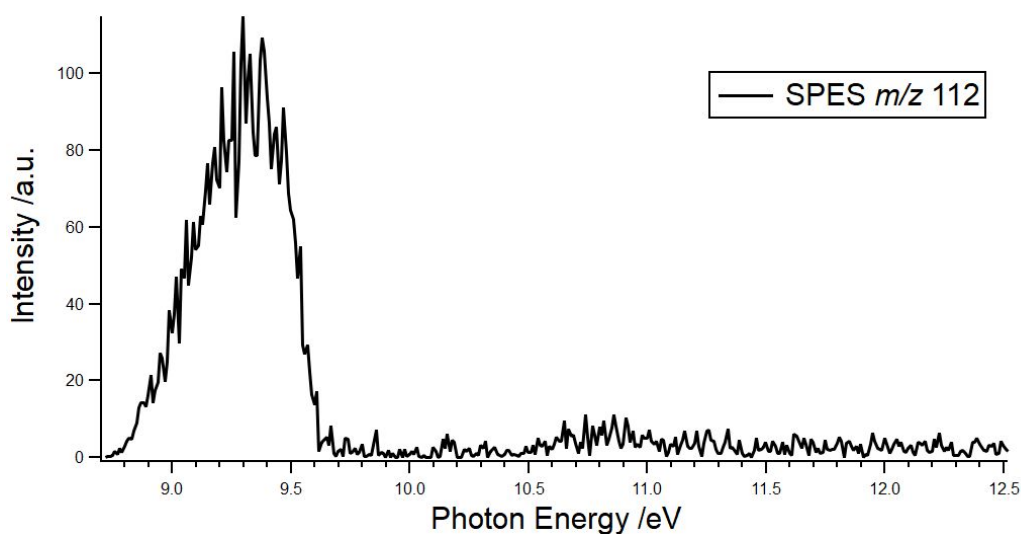
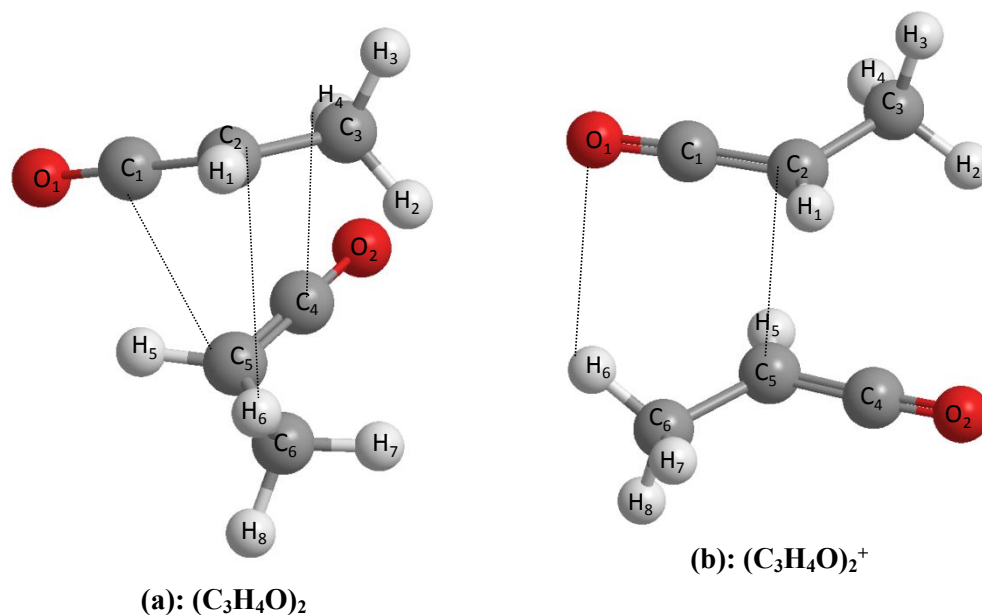


Figure 7. The SPES corresponding to MKE₂ (m/z 112).



384 **Figure 8.** Optimized geometries of MKE₂ (a) and its cation (b).

385 **Table 4.** Bond distances defining the equilibrium molecular structure of MKE₂ and of its cation
 386 in their electronic ground states. These parameters are computed at the PBE0/aug-cc-pVTZ
 387 level of theory. Distances are presented in Å. See Figure 8 for the numbering of the atoms.

	$(C_3H_4O)_2$	$(C_3H_4O)_2^+$
O ₁ -C ₁	1.162	1.140
C ₁ -C ₂	1.307	1.342
C ₂ -C ₃	1.502	1.497
C ₂ -H ₁	1.084	1.087
C ₃ -H ₂	1.093	1.091
C ₃ -H ₃	1.092	1.094
C ₃ -H ₄	1.089	1.088
O ₂ -C ₄	1.162	1.140
C ₄ -C ₅	1.306	1.342
C ₅ -C ₆	1.502	1.496
C ₆ -H ₅	1.083	1.086
C ₆ -H ₆	1.093	1.092
C ₆ -H ₇	1.090	1.088
C ₆ -H ₈	1.092	1.094
C ₂ -C ₅		2.746
O ₁ -H ₆		2.716
C ₄ -H ₄	2.926	
C ₂ -H ₆	3.036	
C ₁ -C ₅	3.383	

388

389 To gain a complete understanding of the dimer's VUV photostability, its dissociative ionization
390 requires the implementation of theoretical calculations. The optimized equilibrium molecular
391 structures of the neutral dimer, MKE_2 , and its cation, MKE_2^+ , are shown in Figure 8 as
392 computed at the PBE0/aug-cc-pVTZ level. All bond distances are summarized in the Table 4.
393 As can be seen, the structure of MKE_2 undergoes a significant geometry change upon ionization.
394 These changes are at the origin of the unfavorable FC factors causing the shape of the broad
395 unstructured band in the dimer's SPES. This is perfectly consistent with our expectations from
396 the FC principle.⁴⁵

397

398 **3.3.2 Dissociative photoionization of MKE_2 - formation of m/z 58, 57, 55, 54, 27, 26**

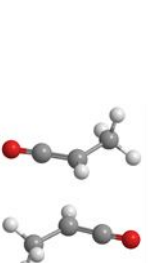
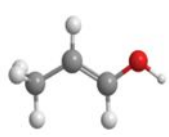
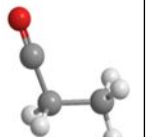
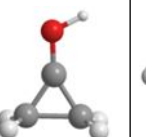
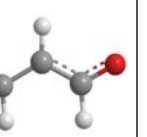
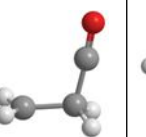
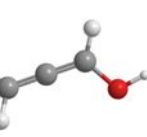
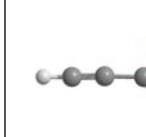
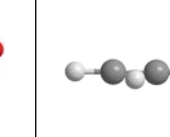
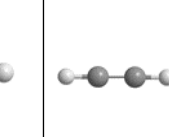
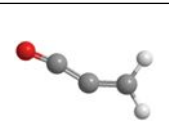
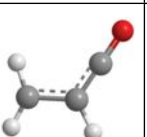
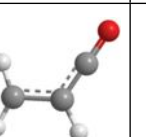
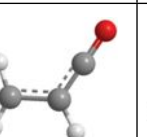
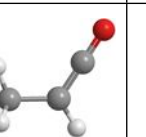
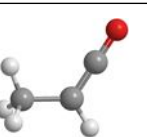
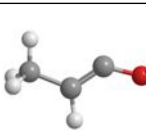
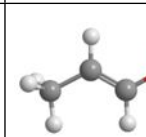
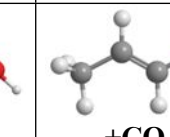
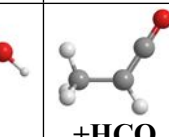
399 The abrupt decrease in the SPES signal of the dimer combined with the optimized geometries
400 of its neutral and cationic forms are an indication of a dissociative ionization process. To gain
401 a clearer understanding of the potential products formed through dissociative ionization of the
402 MKE dimer, various fragmentation channels, presented as a scheme in Figure 9, were quantum-
403 chemically investigated. Our theoretical and experimental results are presented in Table 5 where
404 values of the respective AEs together with the AIE of MKE_2 are tabulated. Further
405 computational details are given in Table S7 of the SI.

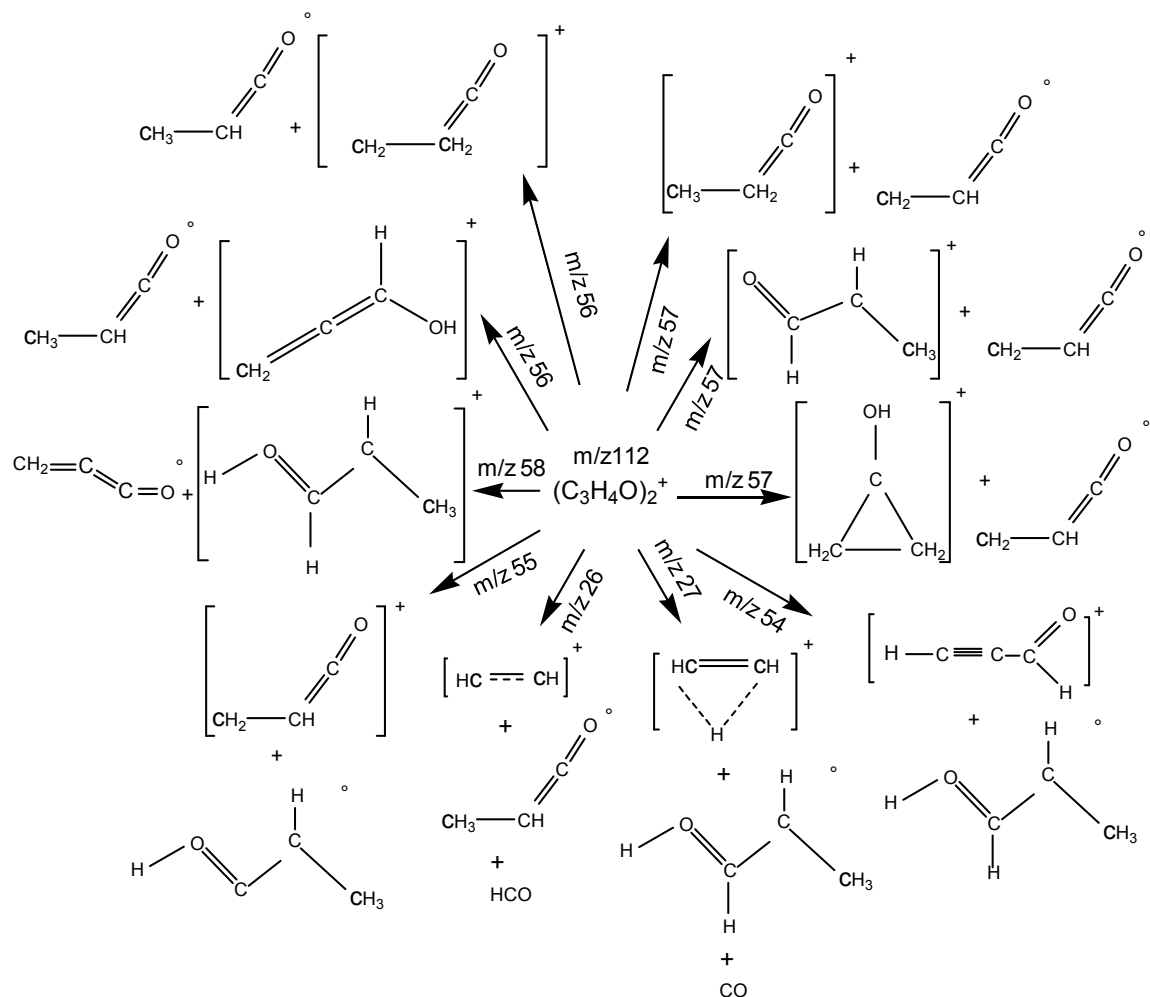
406 There is a large discrepancy between the measured and the calculated AIE of MKE_2
407 (about 0.9 eV), where the theoretical value is lower than the experimental one by ~ 0.9 eV. This
408 comes from the large changes, at least, on the intermonomer distances which shrink upon
409 ionization. Consequently, we expect unfavorable FC factors for population of the low
410 vibrational bands of the dimer cation. Indeed, upon ionization of neutral van der Waals clusters,
411 the ground state vibrational levels of the ionic cluster are commonly located outside the FC-
412 region accessible via direct photoionization of the neutral dimer.⁶² The Ar_2^+ dimer has been
413 resolved with the SPES method⁶⁸ but a prerequisite is a clear trend in the vibrational envelope
414 which we do not observe in MKE_2 which precludes an experimental determination of the true
415 AIE.

416 The calculations on the MKE_2 fragmentation show that a few different products can be
417 obtained from dissociative ionization of the dimer. One product, corresponding formally to the
418 addition of two H-atoms to the MKE monomer (m/z 58) is expected to form around 9.62 eV.
419 Its elemental formula is $\text{C}_3\text{H}_6\text{O}^+$ and the calculated structure is given in Table 5. Another
420 product is m/z 57 and three different isomers corresponding formally to protonated forms of
421 MKE are expected theoretically at 8.78 eV, 10.11 eV, and 11.47 eV. Also m/z 55 can be formed

422 from the dissociative photoionization of MKE_2 . In the following we discuss the formation of
423 these three ions.

424 **Table 5.** Calculated and measured AIEs of MKE₂ and the AEs of the different fragmentation pathways of the resulting cation (in eV). The * labels
 425 correspond to fragments that were also reported in Table 4 as potential fragments from dissociative ionization of the MKE monomer. However,
 426 our computational results shown here indicate that these fragments are more likely formed from dissociative ionization of the MKE₂ dimer. See
 427 text for details.
 428

	Neutral	Ionization	Fragments									
Formula	(C ₃ H ₄ O) ₂	(C ₃ H ₄ O) ₂ ⁺	C ₃ H ₆ O ⁺	C ₃ H ₅ O ⁺	C ₃ H ₅ O ⁺ _1	C ₃ H ₅ O ⁺ _2	C ₃ H ₄ O ⁺	C ₃ H ₄ O ⁺ _1	C ₃ H ₃ O ⁺	C ₃ H ₂ O ⁺	C ₂ H ₃ ⁺	C ₂ H ₂ ⁺
Molecular structure												
			C ₃ H ₂ O	C ₃ H ₃ O	C ₃ H ₃ O	C ₃ H ₃ O	C ₃ H ₄ O	C ₃ H ₄ O	C ₃ H ₅ O	C ₃ H ₆ O	C ₃ H ₆ O	C ₃ H ₄ O
												
<i>m/z</i>		112	58	57	57	57	56	56	55	54*	27*	26*
AIE or AE Calc.		7.87	9.62	8.78	10.11	11.47	10.20	11.41	10.28	12.18	13.05	13.01
AIE or AE Exptl.		8.75 ± 0.05	9.718 ± 0.05	<9.0	10.10 ± 0.05	11.35 ± 0.05	10.20 ± 0.05	11.35 ± 0.05	10.30 ± 0.05	12.3 ± 0.1	13.1 ± 0.1	12.9 ± 0.1



430

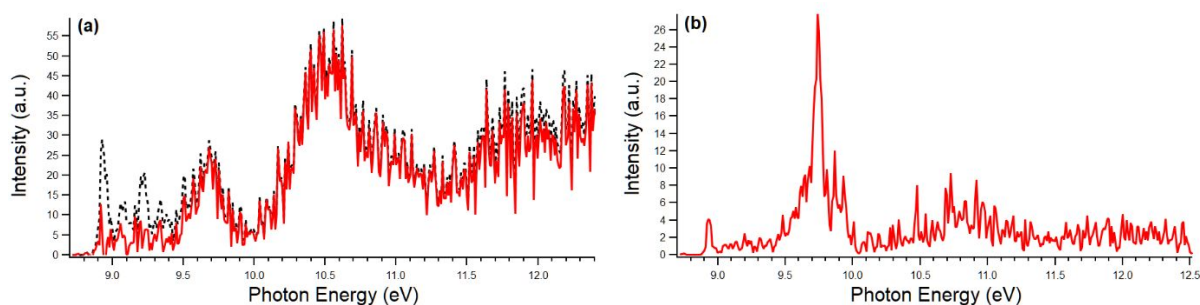
431 **Figure 9.** Fragmentation pathways of the dimer cation MKE_2^+ considered for the quantum-
 432 chemical calculations.

433

434 The SPES associated with $m/z 57$ and $m/z 58$ ions are displayed in Figure 10. As
 435 expected, a slight contribution of the ^{13}C isotopomer signal of the MKE monomer is observed
 436 in the $m/z 57$ SPES which is presented as a dotted black line in Figure 10a. With step sizes of
 437 10 meV in the energy scan, we can safely make the assumption that any decipherable isotopic
 438 shift due to ^{13}C is minimal and we can use the SPES of the monomer at $m/z 56$ to subtract the
 439 ^{13}C signal from the total $m/z 57$ signal, yielding the filtered signal corresponding to the
 440 protonated parent only. This is presented as a solid red line in Figure 10a. This filtered signal
 441 still exhibits some weak signals around and below 9.0 eV which may be an indicator of the
 442 formation of the $m/z 57$ isomer predicted with $AE = 8.78$ eV, namely, the propenoyl cation (see
 443 Table 5).

444 In the SPES of the $m/z 57$ ion three bands are observed peaking at approximately 9.7,
 445 10.6, and 11.9 eV. The calculations predict cyclopropanol-1-yl to appear at $AE = 10.11$ eV
 446 which agrees with the SPES since this is the onset of the second broad band that extends up to

447 approximately 11.35 eV. Furthermore, the calculations predict the appearance of propanal-2-yl
 448 at AE = 11.47 eV, which is also in good agreement with the recorded SPES since this is the
 449 origin of the third broad band observed in the SPES. The first broad band, occurring between
 450 9.5 eV and 10.0 eV, can be explained by the following considerations: Its onset is unlikely to
 451 belong to the propanoyl radical (AE = 8.78 eV), but we note that the first band in the filtered
 452 m/z 57 SPES is quite similarly shaped as the second one that had been assigned to the formation
 453 of cyclopropanol-1-yl cation above, only less intense. It is therefore quite likely that first band
 454 peaking at 9.7 eV corresponds to the same isomeric cation, only originating from a larger cluster
 455 than the dimer. It is quite possible that this band corresponds to the formation of ionized
 456 cyclopropanol-1-yl from the dissociative ionization of the trimer, whose signal abruptly cuts
 457 off at 9.5 eV (see Figure S3 in the SI). No quantum calculations were carried out for the trimer,
 458 so a computational verification of this awaits later work.



460
 461 **Figure 10.** SPES of the (a) m/z 57 and (b) m/z 58 fragments formed by dissociation
 462 photoionization of the MKE dimer are presented in red. In panel (a), the m/z 57 signal which
 463 includes both the ^{13}C isotopomer signal of the MKE parent and the protonated MKE parent is
 464 displayed with the dotted black line. See text for details.

465
 466 Figure 10b presents the SPES of m/z 58. There is a sharp band peaking at 9.72 ± 0.05
 467 eV. With the help of the calculations it can be assigned nicely to the formation of ionized (E)-
 468 1-propenol, $\text{C}_3\text{H}_6\text{O}^+$ predicted to appear at AE = 9.62 eV from the dissociative photoionization
 469 of MKE_2 .

470 From the optimized structure of the neutral dimer and the fragments formed by
 471 dissociative ionization we can infer a few potential mechanisms: The optimized geometry of
 472 the m/z 58 fragment implies a mechanism akin to H_2 addition over the $\text{C}=\text{O}$ double bond. The
 473 structure corresponds to ionized (E)-1-propenol and a likely formation mechanism might
 474 involve the H2 and H4 atoms in Figure 8a dissociating from C3 in the upper neutral monomer
 475 and form covalent bonds with the O2 and C4 atoms in the monomer below. We suggest this

476 mechanism because the location of the carbonyl group in the upper monomer is too far apart
477 from the closest-located H-atoms in the monomer below, to allow for a facile double H-atom
478 addition.

479 For the three m/z 57 isomers predicted by the calculations we observe two of them
480 definitively in the recorded SPES. The strongest feature in the SPES has been assigned to the
481 formation of the cyclopropanol-1-yl cation. From the optimized geometries in Figure 8a, the
482 likeliest formation mechanism would involve a ring-closing between C4 and C6 in the lower
483 monomer while the O2 atom abstracts the H2 atom from the upper monomer. The other m/z 57
484 isomer we observe in the SPES, namely propanal-2-yl cation, requires the abstraction of an H-
485 atom by the carbonyl C-atom. This is most likely easily facilitated in the bottom monomer of
486 the neutral where the C4 atom abstracts the H4 atom from the upper monomer.

487 The ion observed at m/z 55 that is formed from the monomer MKE^+ by H loss reaction
488 (see above) can also be formed by dissociative photoionization of MKE_2 . Contrary to the AE
489 calculation for the $\text{MKE} + h\nu \rightarrow \text{H} + \text{C}_3\text{H}_3\text{O}^+$ reaction (see Table 3) in the calculations for the
490 $\text{MKE}_2 + h\nu \rightarrow \text{C}_3\text{H}_5\text{O} + \text{C}_3\text{H}_3\text{O}^+$ reaction, two isomers for the neutral fragment $\text{C}_3\text{H}_3\text{O}$ have to
491 be considered giving rise to two different AE values, at 9.06 eV and 10.28 eV respectively (see
492 Table 5). As mentioned above and shown in Figure 4, there was some weak structure observed
493 in the SPES of m/z 55, with an experimentally observed onset found at $\text{AE}_a = 10.30 \pm 0.05$ eV.
494 This threshold could not be explained by dissociative ionization of the MKE monomer. Our
495 calculations, however, provide us with an explanation of this spectral feature since AE_a (m/z
496 55) coincides nicely with the formation of the ionized propenoyl radical according to $\text{MKE}_2 +$
497 $h\nu \rightarrow \text{C}_3\text{H}_5\text{O} + \text{C}_3\text{H}_3\text{O}^+$, calculated to appear at $\text{AE}_{\text{calc}} = 10.28$ eV.

498 Finally, the m/z 54, 27 and 26 experimental appearance energies match the theoretical
499 values for the dissociative ionization and subsequent fragmentation of the MKE dimer rather
500 than the monomer.

501

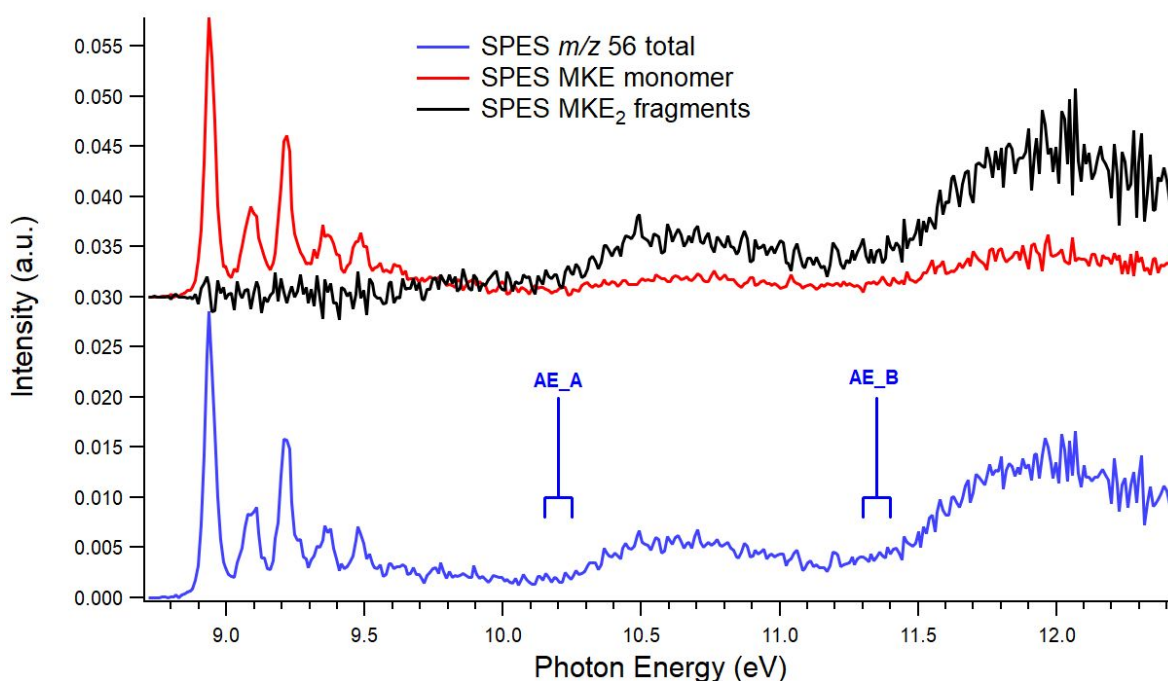
502 3.2.3 Dissociative photoionization of the MKE dimer - m/z 56

503 Unimolecular dissociation of the MKE dimer is also expected to result in fragments with
504 the same elemental formula as the monomer, i.e. $\text{C}_3\text{H}_4\text{O}^+$. Indeed, when the entire m/z 56 peak
505 from Figure 1 was treated, some curious broad unresolved signals appeared at energies above
506 the ground state, between 10 and 12.5 eV (labelled AE_A and AE_B , respectively in Figure
507 11). Prior PES measurements show that the first excited state of the cation does not appear until
508 13.3 eV.¹⁶ Our computations at the MRCI/aVTZ level verify this as they find that the first

509 excited state for the MKE^+ ion is located 4.6 eV above neutral MKE ground state (See Table
510 S8). This means that other ways had to be found to successfully disentangle the SPES of the
511 MKE parent ion for photon energies in the 9.5-13.3 eV Franck-Condon gap.

512 The m/z 56 peak undergoes a significant broadening at higher energies (see Figure S4)
513 and hence we derived a SPES analyzing just the center of the mass peak as well as the total
514 mass peak. The results of this treatment are presented in Figure 11. We find that the difference
515 between the two treatments left the broad signals (AE_A and AE_B) untouched while the SPES
516 of the monomer ground state was successfully filtered away (cf. black line in the upper panel
517 of Fig. 11). The same treatment was applied to the total ion yield (TIY) of the m/z 56 signal to
518 obtain the TIY curves of MKE individually and the other $\text{C}_3\text{H}_4\text{O}$ fragments (Figure S5).

519



520
521 **Figure 11.** Lower panel: SPES of the entire m/z 56 mass peak (cf. Figure 1a; blue line). Upper
522 panel: SPES of the center of the m/z 56 mass peak (red line). Difference spectrum of both
523 treatments (black line). For further explanations, see text. The pattern observed in the lower
524 panel could correspond to the formation of isomers of the parent ions from the noncovalent
525 dimer (See Table 5). Two onsets (AE_A and AE_B) are indicated. For further explanations, see
526 text.

527

528 To assign the broad bands of the difference spectrum we performed additional quantum
529 calculations to account for the dissociation of the dimer back into other isomers of $\text{C}_3\text{H}_4\text{O}^+$. The
530 results of these calculations are presented in Table S5. The calculations predict AEs of two

531 isomers, namely the ionized $\text{CH}_2\text{CH}_2\text{CO}$ biradical, at $\text{AE} = 10.20$ eV, and ionized
532 hydroxypropadiene ($\text{CH}_2=\text{C}=\text{CHOH}$), at $\text{AE} = 11.41$ eV. The appearance energies calculated
533 for the formation of these two $\text{C}_3\text{H}_4\text{O}^+$ isomers coincide very well with the origin of the broad
534 bands of the difference spectrum presented in Figure 11, at approximately 10.20 eV and 11.35
535 eV. Again, the calculations complement the experiment very well to account for the broad
536 signals observed in the m/z 56 SPES.

537

538 4. ASTROCHEMICAL IMPLICATIONS

539 The simplest molecule to contain a CCO frame, namely ketene, was detected in Sgr B2 with
540 the NRAO 11-m telescope in a dense region within the Sgr B2 cloud but with relatively low
541 column densities, i.e. around 10^{14} cm^{-2} .¹⁵ Ketene is the most stable molecular form of $\text{C}_2\text{H}_2\text{O}$
542 isomers and the only such isomer to have been detected in the interstellar medium.⁶⁹ In terms
543 of such thermochemistry considerations, recent results may provide some insight which is
544 complemented here by our results. Indeed, our results may hold some significant astrochemical
545 implications regarding the potential presence and fate of MKE in the ISM.

546 As mentioned in the introduction, MKE's isomer propenal has been detected in
547 Sagittarius B2 and TMC-1 along with propanal ($\text{C}_3\text{H}_6\text{O}$).⁷⁰ In the case of propenal, the
548 observations implied a very low temperature (a few K) which precluded an estimate for column
549 densities. Later observations of propenal in the galactic center, however, found abundances
550 around 10^{-9} with respect to H_2 .⁷¹

551 The most stable form of propenal is 2.8 kJ/mol more stable than MKE and based on this
552 reasoning, MKE was a viable candidate for detection in space.¹⁹ However, MKE could not be
553 definitely detected in various interstellar regions, but upper limits to its column densities were
554 obtained for dark clouds in different evolutionary stages such as high-mass star-forming regions
555 or cold dark clouds. The largest value of the upper limit of MKE abundance was found in Sgr
556 B2 where values of $(100 \pm 50) \times 10^{14} \text{ cm}^{-2}$ were inferred. This upper limit is two orders of
557 magnitude larger than the column density of ketene in Sgr B2.

558 This line of thinking, i.e. letting thermodynamic principles guide the search for
559 interstellar molecules has had some successful precedence recently with $\text{C}_3\text{H}_2\text{O}$ structural
560 isomers, however.⁷² Thermodynamically, the most stable form of $\text{C}_3\text{H}_2\text{O}$ is found to be
561 propadienone (CH_2CCO – also including the same CCO frame as MKE) but it has continued to
562 elude observations.^{73,74} By utilizing quantum chemical calculations it was found that its reaction
563 with a H-atom is barrierless and thus it is now predicted that propadienone undergoes

564 subsequent H-atom additions on grain surfaces to give rise to propenal.⁷² whose presence in Sgr
565 B2 is well established.

566 In comparison with the non-detection of MKE, it is possible that if H-atom addition to
567 MKE is barrierless as well, then this could be a contributing factor for why MKE has eluded
568 detection so far. Thus prior to desorption from the grain mantle, MKE may react without
569 barriers with two H atoms to form a C₃H₆O isomer - either propanal or 1-propenol
570 (CH₃CHCHOH). 1-propenol exists in two different conformers, namely (E)- and (Z)-1-
571 propenol, neither of which has been detected in space, while the presence of propanal, however,
572 is well documented in Sgr B2.⁷⁰ For absolute confirmation, this awaits future work.

573 Our results, however, give way to another potential scenario for why MKE has eluded
574 detection so far. The ionization energy of MKE is below the Lyman- α limit and hence it is
575 possible that ionization by interstellar VUV radiation depletes the column densities of neutral
576 MKE molecules in these molecular clouds to an extent that they are too small for a definitive
577 detection. We find that the lowest threshold for dissociative ionization is 10.5 eV which gives
578 rise to C₂H₄⁺ and CO fragments. However, this fragmentation channel does not seem to be very
579 intense and other fragmentation channels (e.g. H-loss) could only be reached at higher photon
580 energies. Above 12 eV a wealth of smaller organics can be formed; many of which have already
581 been detected in molecular clouds, but for that reason, their detections cannot be used as any
582 kinds of benchmarks to infer the presence of MKE.

583 In summary, we present two potentially contributing scenarios for why MKE has not
584 been successfully detected in the ISM. (i) It is hydrogenated prior to desorption and accounting
585 for an increase in the abundance of either propanal or the potential existence of interstellar 1-
586 propenol. Alternatively, (ii) it is ionized by cosmic ray induced photons to such an extent that
587 its (perhaps already small) abundance is further depleted.

588 Regarding the potential dust-grain formation of MKE, it is widely regarded that
589 formation of COMs in Sgr B2 mostly takes place on dust grains and that two-body gas phase
590 reactions are of limited importance.⁷⁰ MKE has already been detected as the product of ice
591 mixtures such as C₃H₆ and CO₂ which have undergone VUV irradiation to induce ice
592 chemistry²⁰ but definitive formation mechanisms still remain elusive. If solid-state MKE
593 formation is sufficiently efficient on dust grains in Sgr B2 (or other interstellar regions), then
594 one remaining question is whether its desorption mechanism is efficient.

595 In the laboratory ice study where the formation of MKE was tentatively observed,
596 Hudson *et al.*²⁰ based their assignments on prior experience with ketene formation in similar
597 ice experiments.⁷⁵ Therein, a weak IR feature at 2113 cm⁻¹ was observed to stay in the spectra

598 upon heating the ices up to 150 K. With the spectral feature remaining during this warm-up
599 phase might indicate that MKE may not desorb as efficiently from interstellar ices than other
600 organic species in star-forming regions such as Sgr B2.

601 The question then remains whether the formation yields are high enough that
602 photodesorption of interstellar ice grains containing MKE is sufficient to seed interstellar space
603 with enough MKE for a positive detection. In any case, an active search for the MKE⁺ cation,
604 which is reasonably stable according to our study, and the (E)- and (Z)-isomers of 1-propenol,
605 could be a worthwhile future mission to further understand the interstellar chemistry of C₃H₄O
606 isomers.

607

608 5. CONCLUSIONS

609 In this work, we studied the single-photon ionization of gas-phase MKE and its dimer by means
610 of VUV synchrotron radiation from 8.7 up to 15.5 eV. In terms of the recorded SPES of MKE,
611 our results here present a significant improvement from previous photoelectron spectra of
612 MKE¹⁶ and can be used for purposes of isomeric disentanglement of the products of interstellar
613 ice analogs.²¹ Furthermore, the FC calculated spectrum of MKE reproduced the recorded SPES
614 very well. Measured ionization and dissociative ionization thresholds have been theoretically
615 reproduced using CCSD(T)-F12/cc-pVTZ-F12 calculations in combination with the CV, SR
616 and ZPE corrections, as suggested in the literature. This methodology has been used earlier with
617 some significant success in recent years.^{23–25} This allowed the assignment of experimentally
618 observed masses to the formation of several products of dissociative photoionization of the
619 MKE monomer and dimer. Moreover, we show that photoionization of the van-der Waals dimer
620 MKE₂ gives rise to intramolecular isomerization, H transfer and subsequent unimolecular
621 fragmentation processes, as evidenced by the SPES of fragments corresponding to the addition
622 of one and two H-atoms to the MKE monomer preceding dissociation of dimer. More
623 specifically, the non-covalent character of the dimer is confirmed as its contribution to the
624 formation of MKE fragments could not be explained by solely investigating the dissociative
625 ionization of the monomer. This was demonstrated by theoretical calculations and was key in
626 unravelling the fragmentation patterns observed in our experiment.

627 In summary, our work showcases the synergy of theoretical and experimental work
628 required to elucidate the photo-induced behavior of MKE and particularly the complications
629 wrought by the dissociative ionization of its dimer. The measured mass spectra, SPES and
630 appearance energies of the products were interpreted with the help of *ab initio* and DFT

631 quantum chemical calculations which highlight the important role theory can play when
632 interpreting experimental data.

633 Finally, we discuss the potential formation and eventual fates of neutral and ionized
634 MKE in interstellar media and provide suggestions for future molecular targets of observation
635 campaigns to gain a deeper understanding of the chemistry of C_3H_4O isomers in space.

636

637 **Conflicts of interest**

638 There are no conflicts of interest to declare.

639

640 **Acknowledgements**

641 This work was supported by the French *Programme National Physique et Chimie du Milieu*
642 *Interstellaire* (PCMI) of CNRS/INSU with INC/INP co-funded by CEA and CNES. We are
643 grateful to the whole SOLEIL staff for provisions of synchrotron radiation under proposal
644 number 20170203, as well to J.-F. Gil for his technical assistance on the SAPHIRS endstation.
645 We thank Gustavo Garcia for precious help during the measurement campaigns. H.R.H. is
646 grateful for support from the Marie Skłodowska Curie actions, proposal ID: 838372. J.-C. G.
647 thanks the Centre National d'Etudes Spatiales (CNES) for financial support.

648 **References:**

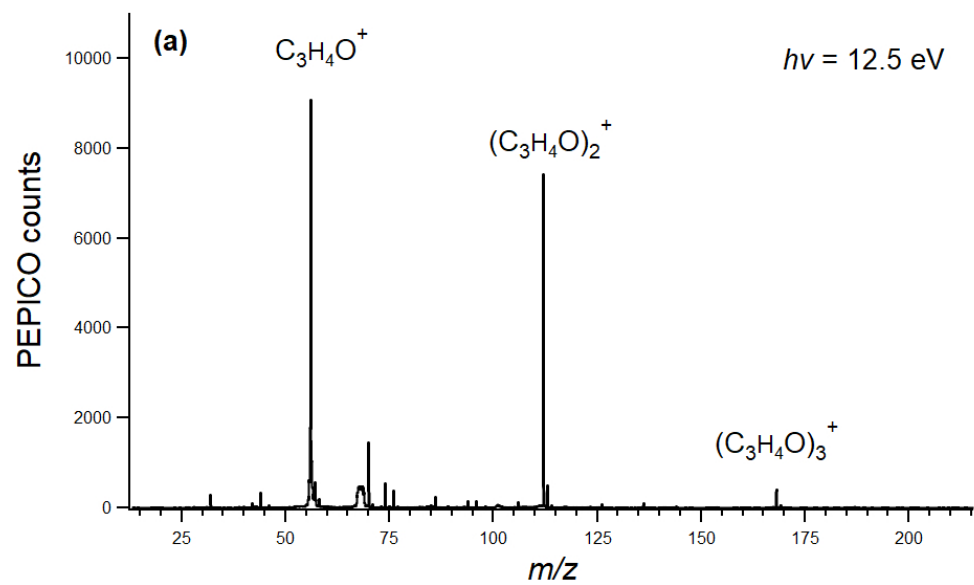
- 649 (1) Öberg, K. I. Photochemistry and Astrochemistry: Photochemical Pathways to Interstellar
650 Complex Organic Molecules. *Chem. Rev.* **2016**, *116* (17), 9631–9663.
651 <https://doi.org/10.1021/acs.chemrev.5b00694>.
- 652 (2) Linnartz, H.; Ioppolo, S.; Fedoseev, G. Atom Addition Reactions in Interstellar Ice Analogues.
653 *International Reviews in Physical Chemistry* **2015**, *34* (2), 205–237.
654 <https://doi.org/10.1080/0144235X.2015.1046679>.
- 655 (3) Herbst, E.; van Dishoeck, E. F. Complex Organic Interstellar Molecules. In *Annual Review of*
656 *Astronomy and Astrophysics*; Blandford, R., Kormendy, J., van Dishoeck, E., Eds.; Annual
657 Reviews: Palo Alto, 2009; Vol. 47, pp 427–480.
- 658 (4) McGuire, B. A. 2018 Census of Interstellar, Circumstellar, Extragalactic, Protoplanetary Disk, and
659 Exoplanetary Molecules. *Astrophys. J. Suppl. Ser.* **2018**, *239* (2), 17.
660 <https://doi.org/10.3847/1538-4365/aae5d2>.
- 661 (5) Paardekooper, D. M.; Bossa, J.-B.; Linnartz, H. Laser Desorption Time-of-Flight Mass
662 Spectrometry of Vacuum UV Photo-Processed Methanol Ice. *A&A* **2016**, *592*, A67.
663 <https://doi.org/10.1051/0004-6361/201527937>.
- 664 (6) Paardekooper, D. M.; Bossa, J.-B.; Isokoski, K.; Linnartz, H. Laser Desorption Time-of-Flight Mass
665 Spectrometry of Ultraviolet Photo-Processed Ices. *Review of Scientific Instruments* **2014**, *85*
666 (10), 104501. <https://doi.org/10.1063/1.4896754>.
- 667 (7) Bertin, M.; Fayolle, E. C.; Romanzin, C.; Poderoso, H. A. M.; Michaut, X.; Philippe, L.; Jeseck, P.;
668 Oeberg, K. I.; Linnartz, H.; Fillion, J.-H. Indirect Ultraviolet Photodesorption from CO:N-2 Binary
669 Ices - An Efficient Grain-Gas Process. *Astrophysical Journal* **2013**, *779* (2).
670 <https://doi.org/10.1088/0004-637X/779/2/120>.
- 671 (8) Öberg, K. I.; Garrod, R. T.; van Dishoeck, E. F.; Linnartz, H. Formation Rates of Complex Organics
672 in UV Irradiated CH₃OH-Rich Ices I. Experiments. *Astronomy & Astrophysics* **2009**, *504* (3), 891-
673 U28. <https://doi.org/10.1051/0004-6361/200912559>.
- 674 (9) Potapov, A.; Canosa, A.; Jimenez, E.; Rowe, B. Uniform Supersonic Chemical Reactors: 30 Years
675 of Astrochemical History and Future Challenges. *Angew. Chem.-Int. Edit.* **2017**, *56* (30), 8618–
676 8640. <https://doi.org/10.1002/anie.201611240>.
- 677 (10) Cooke, I. R.; Sims, I. R. Experimental Studies of Gas-Phase Reactivity in Relation to Complex
678 Organic Molecules in Star-Forming Regions. *ACS Earth Space Chem.* **2019**, *3* (7), 1109–1134.
679 <https://doi.org/10.1021/acsearthspacechem.9b00064>.
- 680 (11) McGuire, B. A.; Burkhardt, A. M.; Kalenskii, S.; Shingledecker, C. N.; Remijan, A. J.; Herbst, E.;
681 McCarthy, M. C. Detection of the Aromatic Molecule Benzonitrile (c-C₆H₅CN) in the Interstellar
682 Medium. *Science* **2018**, *359* (6372), 202–205. <https://doi.org/10.1126/science.aao4890>.
- 683 (12) Linnartz, H.; Cami, J.; Cordiner, M.; Cox, N. L. J.; Ehrenfreund, P.; Foing, B.; Gatchell, M.; Scheier,
684 P. C₆₀⁺ as a Diffuse Interstellar Band Carrier; a Spectroscopic Story in 6 Acts. *Journal of*
685 *Molecular Spectroscopy* **2020**, *367*, 111243. <https://doi.org/10.1016/j.jms.2019.111243>.
- 686 (13) Taniguchi, K.; Miyamoto, Y.; Saito, M.; Sanhueza, P.; Shimoikura, T.; Dobashi, K.; Nakamura, F.;
687 Ozeki, H. Interferometric Observations of Cyanopolynes toward the G28.28–0.36 High-Mass
688 Star-Forming Region. *ApJ* **2018**, *866* (1), 32. <https://doi.org/10.3847/1538-4357/aadd0c>.
- 689 (14) Cordiner, M. A.; Charnley, S. B.; Kisiel, Z.; McGuire, B. A.; Kuan, Y.-J. Deep K-Band Observations
690 of TMC-1 with the Green Bank Telescope: Detection of HC₇O, Non-Detection of HC₁₁N, and a
691 Search for New Organic Molecules. *ApJ* **2017**, *850* (2), 187. <https://doi.org/10.3847/1538-4357/aa970c>.
- 692
693 (15) Turner, B. E. Microwave Detection of Interstellar Ketene. *ApJ* **1977**, *213*, L75.
694 <https://doi.org/10.1086/182413>.
- 695 (16) Bock, H.; Hirabayashi, T.; Mohmand, S. Gas-Phase Reactions .21. Thermal Generation of
696 Alkylketenes and Halogenketenes. *Chem. Ber.-Recl.* **1981**, *114* (7), 2595–2608.
697 <https://doi.org/10.1002/cber.19811140722>.

- 698 (17) Mckee, M.; Radom, L. Structures and Stabilities of $C_3H_4O^+$. Isomers - a G2 Theoretical-Study.
699 *Org. Mass Spectrom.* **1993**, *28* (10), 1238–1244. <https://doi.org/10.1002/oms.1210281040>.
- 700 (18) Winther, F.; Meyer, S.; Nicolaisen, F. M. The Infrared Spectrum of Methylketene. *J. Mol. Struct.*
701 **2002**, *611* (1–3), 9–22. [https://doi.org/10.1016/S0022-2860\(02\)00006-6](https://doi.org/10.1016/S0022-2860(02)00006-6).
- 702 (19) Bermúdez, C.; Tercero, B.; Motiyenko, R. A.; Margulès, L.; Cernicharo, J.; Ellinger, Y.; Guillemin,
703 J.-C. The Millimeter-Wave Spectrum of Methyl Ketene and the Astronomical Search for It. *A&A*
704 **2018**, *619*, A92. <https://doi.org/10.1051/0004-6361/201833267>.
- 705 (20) Hudson, R. L.; Loeffler, M. J.; Yocum, K. M. Laboratory Investigations into the Spectra and Origin
706 of Propylene Oxide: A Chiral Interstellar Molecule. *ApJ* **2017**, *835* (2), 225.
707 <https://doi.org/10.3847/1538-4357/835/2/225>.
- 708 (21) Abplanalp, M. J.; Foerstel, M.; Kaiser, R. I. Exploiting Single Photon Vacuum Ultraviolet
709 Photoionization to Unravel the Synthesis of Complex Organic Molecules in Interstellar Ices.
710 *Chem. Phys. Lett.* **2016**, *644*, 79–98. <https://doi.org/10.1016/j.cplett.2015.11.029>.
- 711 (22) Goulay, F.; Trevitt, A. J.; Savee, J. D.; Bouwman, J.; Osborn, D. L.; Taatjes, C. A.; Wilson, K. R.;
712 Leone, S. R. Product Detection of the CH Radical Reaction with Acetaldehyde. *J. Phys. Chem. A*
713 **2012**, *116* (24), 6091–6106. <https://doi.org/10.1021/jp2113126>.
- 714 (23) Bellili, A.; Schwell, M.; Bénilan, Y.; Fray, N.; Gazeau, M.-C.; Mogren Al-Mogren, M.; Guillemin, J.-
715 C.; Poisson, L.; Hochlaf, M. VUV Photoionization and Dissociative Photoionization Spectroscopy
716 of the Interstellar Molecule Aminoacetonitrile: Theory and Experiment. *Journal of Molecular*
717 *Spectroscopy* **2015**, *315*, 196–205. <https://doi.org/10.1016/j.jms.2015.05.008>.
- 718 (24) Bellili, A.; Schwell, M.; Bénilan, Y.; Fray, N.; Gazeau, M.-C.; Mogren Al-Mogren, M.; Guillemin, J.-
719 C.; Poisson, L.; Hochlaf, M. VUV Photoionization and Dissociative Photoionization of the
720 Prebiotic Molecule Acetyl Cyanide: Theory and Experiment. *J. Chem. Phys.* **2014**, *141* (13),
721 134311. <https://doi.org/10.1063/1.4896987>.
- 722 (25) Bellili, A.; Gouid, Z.; Gazeau, M. C.; Bénilan, Y.; Fray, N.; Guillemin, J. C.; Hochlaf, M.; Schwell, M.
723 Single Photon Ionization of Methyl Isocyanide and the Subsequent Unimolecular
724 Decomposition of Its Cation: Experiment and Theory. *Phys. Chem. Chem. Phys.* **2019**, *21* (47),
725 26017–26026. <https://doi.org/10.1039/C9CP04310A>.
- 726 (26) Chen, Z.; Lau, K.-C.; Garcia, G. A.; Nahon, L.; Božanić, D. K.; Poisson, L.; Al-Mogren, M. M.;
727 Schwell, M.; Francisco, J. S.; Bellili, A.; Hochlaf, M. Identifying Cytosine-Specific Isomers via
728 High-Accuracy Single Photon Ionization. *J. Am. Chem. Soc.* **2016**, *138* (51), 16596–16599.
729 <https://doi.org/10.1021/jacs.6b10413>.
- 730 (27) Derbali, I.; Hrodmarsson, H. R.; Gouid, Z.; Schwell, M.; Gazeau, M.-C.; Guillemin, J.-C.; Hochlaf,
731 M.; Alikhani, M. E.; Zins, E.-L. Photoionization and Dissociative Photoionization of Propynal in
732 the Gas Phase: Theory and Experiment. *Physical Chemistry Chemical Physics* **2019**, *21* (26),
733 14053–14062. <https://doi.org/10.1039/c8cp06751a>.
- 734 (28) Gouid, Z.; Röder, A.; Cunha de Miranda, B. K.; Gaveau, M.-A.; Briant, M.; Soep, B.; Mestdagh, J.-
735 M.; Hochlaf, M.; Poisson, L. Energetics and Ionization Dynamics of Two Diarylketone Molecules:
736 Benzophenone and Fluorenone. *Phys. Chem. Chem. Phys.* **2019**, *21* (26), 14453–14464.
737 <https://doi.org/10.1039/C9CP02385B>.
- 738 (29) Majdi, Y.; Hochlaf, M.; Pan, Y.; Lau, K.-C.; Poisson, L.; Garcia, G. A.; Nahon, L.; Al-Mogren, M. M.;
739 Schwell, M. Theoretical and Experimental Photoelectron Spectroscopy Characterization of the
740 Ground State of Thymine Cation. *J. Phys. Chem. A* **2015**, *119* (23), 5951–5958.
741 <https://doi.org/10.1021/jp510716c>.
- 742 (30) Nahon, L.; de Oliveira, N.; Garcia, G. A.; Gil, J.-F.; Pilette, B.; Marcouille, O.; Lagarde, B.; Polack,
743 F. DESIRS: A State-of-the-Art VUV Beamline Featuring High Resolution and Variable Polarization
744 for Spectroscopy and Dichroism at SOLEIL. *Journal of Synchrotron Radiation* **2012**, *19* (4), 508–
745 520. <https://doi.org/10.1107/S0909049512010588>.
- 746 (31) Marcouille, O.; Brunelle, P.; Chubar, O.; Marteau, F.; Massal, M.; Nahon, L.; Tavakoli, K.;
747 Veteran, J.; Filhol, J.-M. Design, Construction and Magnetic Measurements of the HU640
748 (OPHELIE2) Undulator Dedicated to the DESIRS VUV Beamline at SOLEIL. In *Synchrotron*
749 *Radiation Instrumentation Pts 1 & 2*; Choi, JY and Rah, S, Ed.; AIP Conference Proceedings;

- 750 American Institute of Physics: 2 Huntington Quadrangle, Ste 1No1, Melville, NY 11747-4501
751 USA, 2007; Vol. 879, p 311+.
- 752 (32) Tang, X.; Garcia, G. A.; Gil, J.-F.; Nahon, L. Vacuum Upgrade and Enhanced Performances of the
753 Double Imaging Electron/Ion Coincidence End-Station at the Vacuum Ultraviolet Beamline
754 DESIRS. *Review of Scientific Instruments* **2015**, *86* (12). <https://doi.org/10.1063/1.4937624>.
- 755 (33) Garcia, G. A.; de Miranda, B. K. C.; Tia, M.; Daly, S.; Nahon, L. DELICIOUS III: A Multipurpose
756 Double Imaging Particle Coincidence Spectrometer for Gas Phase Vacuum Ultraviolet
757 Photodynamics Studies. *Review of Scientific Instruments* **2013**, *84* (5).
758 <https://doi.org/10.1063/1.4807751>.
- 759 (34) Garcia, G.; Nahon, L.; Powis, I. Two-Dimensional Charged Particle Image Inversion Using a Polar
760 Basis Function Expansion. *Review of Scientific Instruments* **2004**, *75* (11), 4989–4996.
761 <https://doi.org/10.1063/1.1807578>.
- 762 (35) Pouilly, J. C.; Schermann, J. P.; Nieuwjaer, N.; Lecomte, F.; Gregoire, G.; Desfrancois, C.; Garcia,
763 G. A.; Nahon, L.; Nandi, D.; Poisson, L.; Hochlaf, M. Photoionization of 2-Pyridone and 2-
764 Hydroxypyridine. *Phys. Chem. Chem. Phys.* **2010**, *12* (14), 3566–3572.
765 <https://doi.org/10.1039/b923630a>.
- 766 (36) Hrodmarsson, H. R.; Garcia, G. A.; Linnartz, H.; Nahon, L. VUV Photoionization Dynamics of the
767 C₆₀ Buckminsterfullerene: 2D-Matrix Photoelectron Spectroscopy in an Astrophysical Context.
768 *Phys. Chem. Chem. Phys.* **2020**, *22*, 13880–13892. <https://doi.org/10.1039/DOCP01210F>.
- 769 (37) Hrodmarsson, H. R.; Garcia, G. A.; Nahon, L.; Loison, J.-C.; Gans, B. Threshold Photoelectron
770 Spectrum of the Anilino Radical. *The Journal of Physical Chemistry A* **2019**, *123* (42), 9193–9198.
771 <https://doi.org/10.1021/acs.jpca.9b07273>.
- 772 (38) Adamo, C.; Barone, V. Toward Reliable Density Functional Methods without Adjustable
773 Parameters: The PBE0 Model. *J. Chem. Phys.* **1999**, *110* (13), 6158–6170.
774 <https://doi.org/10.1063/1.478522>.
- 775 (39) Dunning, T. Gaussian-Basis Sets for Use in Correlated Molecular Calculations .1. the Atoms
776 Boron Through Neon and Hydrogen. *J. Chem. Phys.* **1989**, *90* (2), 1007–1023.
777 <https://doi.org/10.1063/1.456153>.
- 778 (40) Kendall, R.; Dunning, T.; Harrison, R. Electron-Affinities of the 1st-Row Atoms Revisited -
779 Systematic Basis-Sets and Wave-Functions. *J. Chem. Phys.* **1992**, *96* (9), 6796–6806.
780 <https://doi.org/10.1063/1.462569>.
- 781 (41) Mills, I. M. Potential Energy Surfaces and Vibrational Anharmonicity. In *Recent Experimental*
782 *and Computational Advances in Molecular Spectroscopy*; Fausto, R., Ed.; NATO ASI Series;
783 Springer Netherlands: Dordrecht, 1993; pp 79–98. [https://doi.org/10.1007/978-94-011-1974-](https://doi.org/10.1007/978-94-011-1974-0_5)
784 [0_5](https://doi.org/10.1007/978-94-011-1974-0_5).
- 785 (42) Aliev, M. R.; Watson, J. K. G. Chapter 1 - Higher-Order Effects in the Vibration–Rotation Spectra
786 of Semirigid Molecules. In *Molecular Spectroscopy: Modern Research*; Rao, K. N., Ed.; Academic
787 Press, 1985; pp 1–67. <https://doi.org/10.1016/B978-0-12-580643-5.50006-3>.
- 788 (43) Frisch, M. J.; Trucks, G. W.; Schlegel, H. B.; Scuseria, G. E.; Robb, M. A.; Cheeseman, J. R.;
789 Nakatsuji, H. *Gaussian 09, Revision E.01*; Gaussian Inc. Wallingford, 2009.
- 790 (44) Lax, M. The Franck-Condon Principle and Its Application to Crystals. *J. Chem. Phys.* **1952**, *20*
791 (11), 1752–1760. <https://doi.org/10.1063/1.1700283>.
- 792 (45) Barone, V.; Bloino, J.; Biczysko, M. Vibrationally-Resolved Electronic Spectra in GAUSSIAN 09.
793 *20*.
- 794 (46) Bloino, J.; Biczysko, M.; Santoro, F.; Barone, V. General Approach to Compute Vibrationally
795 Resolved One-Photon Electronic Spectra. *J. Chem. Theory Comput.* **2010**, *6* (4), 1256–1274.
796 <https://doi.org/10.1021/ct9006772>.
- 797 (47) Barone, V.; Bloino, J.; Biczysko, M.; Santoro, F. Fully Integrated Approach to Compute
798 Vibrationally Resolved Optical Spectra: From Small Molecules to Macrosystems. *J. Chem.*
799 *Theory Comput.* **2009**, *5* (3), 540–554. <https://doi.org/10.1021/ct8004744>.

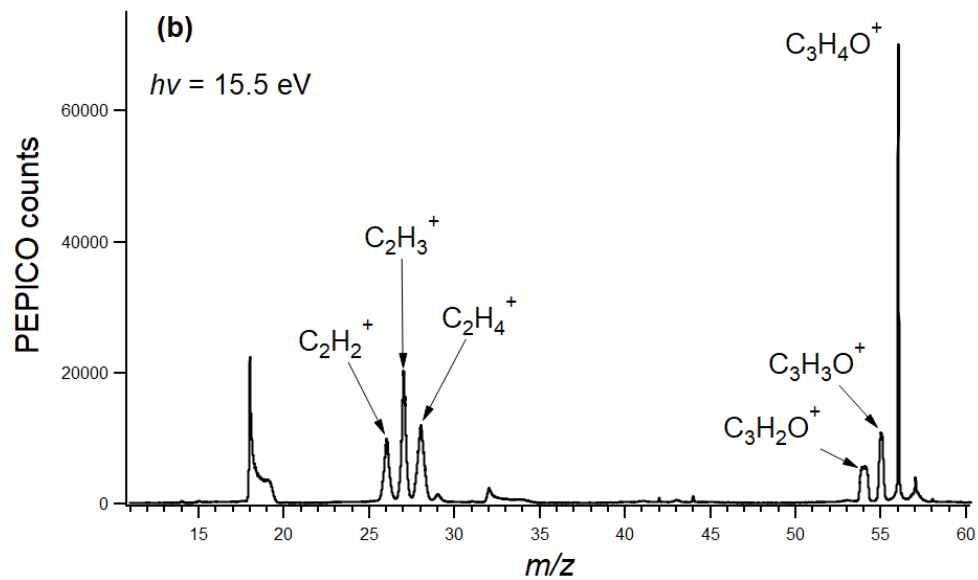
- 800 (48) Bloino, J.; Biczysko, M.; Crescenzi, O.; Barone, V. Integrated Computational Approach to
801 Vibrationally Resolved Electronic Spectra: Anisole as a Test Case. *J. Chem. Phys.* **2008**, *128* (24),
802 244105. <https://doi.org/10.1063/1.2943140>.
- 803 (49) Bloino, J.; Baiardi, A.; Biczysko, M. Aiming at an Accurate Prediction of Vibrational and
804 Electronic Spectra for Medium-to-Large Molecules: An Overview. *Int. J. Quantum Chem.* **2016**,
805 *116* (21), 1543–1574. <https://doi.org/10.1002/qua.25188>.
- 806 (50) Adler, T. B.; Knizia, G.; Werner, H.-J. A Simple and Efficient CCSD(T)-F12 Approximation. *J. Chem.*
807 *Phys.* **2007**, *127* (22), 221106. <https://doi.org/10.1063/1.2817618>.
- 808 (51) Knizia, G.; Adler, T. B.; Werner, H.-J. Simplified CCSD(T)-F12 Methods: Theory and Benchmarks.
809 *J. Chem. Phys.* **2009**, *130* (5), 054104. <https://doi.org/10.1063/1.3054300>.
- 810 (52) Adler, T. B.; Werner, H.-J.; Manby, F. R. Local Explicitly Correlated Second-Order Perturbation
811 Theory for the Accurate Treatment of Large Molecules. *J. Chem. Phys.* **2009**, *130* (5), 054106.
812 <https://doi.org/10.1063/1.3040174>.
- 813 (53) Adler, T. B.; Werner, H.-J. Local Explicitly Correlated Coupled-Cluster Methods: Efficient
814 Removal of the Basis Set Incompleteness and Domain Errors. *J. Chem. Phys.* **2009**, *130* (24),
815 241101. <https://doi.org/10.1063/1.3160675>.
- 816 (54) Koehn, A.; Tew, D. P. Explicitly Correlated Coupled-Cluster Theory Using Cusp Conditions. I.
817 Perturbation Analysis of Coupled-Cluster Singles and Doubles (CCSD-F12). *J. Chem. Phys.* **2010**,
818 *133* (17), 174117. <https://doi.org/10.1063/1.3496372>.
- 819 (55) Werner, H.-J.; Knowles, P. J.; Knizia, G.; Manby, F. R.; Schütz, M.; Celani, P.; Györfy, W.; Kats,
820 D.; Korona, T.; Lindh, R.; Mitrushenkov, A.; Rauhut, G.; Shamasundar, K. R.; Adler, T. B.; Amos,
821 R. D.; Bennie, S. J.; Bernhardsson, A.; Berning, A.; Cooper, D. L.; Deegan, M. J. O.; Dobbyn, A. J.;
822 Eckert, F.; Goll, E.; Hampel, C.; Hesselmann, A.; Hetzer, G.; Hrenar, T.; Jansen, G.; Köppl, C.; Lee,
823 S. J. R.; Liu, Y.; Lloyd, A. W.; Ma, Q.; Mata, R. A.; May, A. J.; McNicholas, S. J.; Meyer, W.; III, T. F.
824 M.; Mura, M. E.; Nicklass, A.; O'Neill, D. P.; Palmieri, P.; Peng, D.; Pflüger, K.; Pitzer, R.; Reiher,
825 M.; Shiozaki, T.; Stoll, H.; Stone, A. J.; Tarroni, R.; Thorsteinsson, T.; Wang, M.; Welborn, M.
826 *MOLPRO, Version 2019.2, a Package of Ab Initio Programs*; Cardiff, UK, 2019.
- 827 (56) Peterson, K. A.; Adler, T. B.; Werner, H.-J. Systematically Convergent Basis Sets for Explicitly
828 Correlated Wavefunctions: The Atoms H, He, B–Ne, and Al–Ar. *J. Chem. Phys.* **2008**, *128* (8),
829 084102. <https://doi.org/10.1063/1.2831537>.
- 830 (57) Peterson, K. A.; Dunning, T. H. Accurate Correlation Consistent Basis Sets for Molecular Core-
831 Valence Correlation Effects: The Second Row Atoms Al–Ar, and the First Row Atoms B–Ne
832 Revisited. *J. Chem. Phys.* **2002**, *117* (23), 10548–10560. <https://doi.org/10.1063/1.1520138>.
- 833 (58) de Jong, W. A.; Harrison, R. J.; Dixon, D. A. Parallel Douglas-Kroll Energy and Gradients in
834 NWChem: Estimating Scalar Relativistic Effects Using Douglas-Kroll Contracted Basis Sets. *J.*
835 *Chem. Phys.* **2001**, *114* (1), 48–53. <https://doi.org/10.1063/1.1329891>.
- 836 (59) Watts, J. D.; Gauss, J.; Bartlett, R. J. Coupled-cluster Methods with Noniterative Triple
837 Excitations for Restricted Open-shell Hartree–Fock and Other General Single Determinant
838 Reference Functions. Energies and Analytical Gradients. *J. Chem. Phys.* **1993**, *98* (11), 8718–
839 8733. <https://doi.org/10.1063/1.464480>.
- 840 (60) Douglas, M.; Kroll, N. M. Quantum Electrodynamical Corrections to the Fine Structure of
841 Helium. *Annals of Physics* **1974**, *82* (1), 89–155. [https://doi.org/10.1016/0003-4916\(74\)90333-9](https://doi.org/10.1016/0003-4916(74)90333-9).
- 842
843 (61) Jansen, G.; Hess, B. A. Revision of the Douglas-Kroll Transformation. *Phys. Rev. A* **1989**, *39* (11),
844 6016–6017. <https://doi.org/10.1103/PhysRevA.39.6016>.
- 845 (62) Hochlaf, M. Advances in Spectroscopy and Dynamics of Small and Medium Sized Molecules and
846 Clusters. *Phys. Chem. Chem. Phys.* **2017**, *19* (32), 21236–21261.
847 <https://doi.org/10.1039/C7CP01980G>.
- 848 (63) Jonkman, H. T.; Even, U.; Kommandeur, J. Clusters of Organic Molecules in a Supersonic Jet
849 Expansion. *J. Phys. Chem.* **1985**, *89* (20), 4240–4243. <https://doi.org/10.1021/j100266a018>.

- 850 (64) Bak, B.; Christiansen, J. J.; Kunstmann, K.; Nygaard, L.; Rastrup-Andersen, J. Microwave
851 Spectrum, Molecular Structure, Barrier to Internal Rotation, and Dipole Moment of
852 Methylketene. *J. Chem. Phys.* **1966**, *45* (3), 883–887. <https://doi.org/10.1063/1.1727700>.
- 853 (65) Mahjoub, A.; Hochlaf, M.; Poisson, L.; Nieuwjaer, N.; Lecomte, F.; Schermann, J.-P.; Grégoire,
854 G.; Manil, B.; Garcia, G. A.; Nahon, L. Slow Photoelectron Spectroscopy of δ -Valerolactam and
855 Its Dimer. *ChemPhysChem* **2011**, *12* (10), 1822–1832. <https://doi.org/10.1002/cphc.201100090>.
- 856 (66) Mahjoub, A.; Hochlaf, M.; Garcia, G. A.; Nahon, L.; Poisson, L. State-Selected Unimolecular
857 Decomposition of δ -Valerolactam⁺ and δ -Valerolactam₂⁺ Cations: Theory and Experiment. *J.*
858 *Phys. Chem. A* **2012**, *116* (34), 8706–8712. <https://doi.org/10.1021/jp3056976>.
- 859 (67) Guan, J.; Hu, Y.; Zou, H.; Cao, L.; Liu, F.; Shan, X.; Sheng, L. Competitive Fragmentation Pathways
860 of Acetic Acid Dimer Explored by Synchrotron VUV Photoionization Mass Spectrometry and
861 Electronic Structure Calculations. *J. Chem. Phys.* **2012**, *137* (12), 124308.
862 <https://doi.org/10.1063/1.4754273>.
- 863 (68) Briant, M.; Poisson, L.; Hochlaf, M.; de Pujo, P.; Gaveau, M.-A.; Soep, B. Ar 2 Photoelectron
864 Spectroscopy Mediated by Autoionizing States. *Phys. Rev. Lett.* **2012**, *109* (19), 193401.
865 <https://doi.org/10.1103/PhysRevLett.109.193401>.
- 866 (69) Etim, E. E.; Gorai, P.; Das, A.; Arunan, E. Theoretical Investigation of Interstellar C–C–O and C–
867 O–C Bonding Backbone Molecules. *Astrophys Space Sci* **2018**, *363* (1), 6.
868 <https://doi.org/10.1007/s10509-017-3226-5>.
- 869 (70) Hollis, J. M.; Jewell, P. R.; Lovas, F. J.; Remijan, A.; Møllendal, H. Green Bank Telescope
870 Detection of New Interstellar Aldehydes: Propenal and Propanal. *ApJ* **2004**, *610* (1), L21–L24.
871 <https://doi.org/10.1086/423200>.
- 872 (71) Requena-Torres, M. A.; Martin-Pintado, J.; Martin, S.; Morris, M. R. The Galactic Center: The
873 Largest Oxygen-bearing Organic Molecule Repository. *ApJ* **2008**, *672* (1), 352–360.
874 <https://doi.org/10.1086/523627>.
- 875 (72) Shingledecker, C. N.; Álvarez-Barcia, S.; Korn, V. H.; Kästner, J. The Case of H₂C₃O Isomers,
876 Revisited: Solving the Mystery of the Missing Propadienone. *ApJ* **2019**, *878* (2), 80.
877 <https://doi.org/10.3847/1538-4357/ab1d4a>.
- 878 (73) Loomis, R. A.; McGuire, B. A.; Shingledecker, C.; Johnson, C. H.; Blair, S.; Robertson, A.; Remijan,
879 A. J. Investigating the Minimum Energy Principle in Searches for New Molecular Species—The
880 Case of H₂C₃O Isomers. *ApJ* **2015**, *799* (1), 34. <https://doi.org/10.1088/0004-637X/799/1/34>.
- 881 (74) Loison, J.-C.; Agúndez, M.; Marcelino, N.; Wakelam, V.; Hickson, K. M.; Cernicharo, J.; Gerin, M.;
882 Roueff, E.; Guélin, M. The Interstellar Chemistry of H₂C₃O Isomers. *Mon. Not. R. Astron. Soc.*
883 **2016**, *456* (4), 4101–4110. <https://doi.org/10.1093/mnras/stv2866>.
- 884 (75) Hudson, R. L.; Loeffler, M. J. Ketene Formation in Interstellar Ices: A Laboratory Study. *ApJ*
885 **2013**, *773* (2), 109. <https://doi.org/10.1088/0004-637X/773/2/109>.
- 886



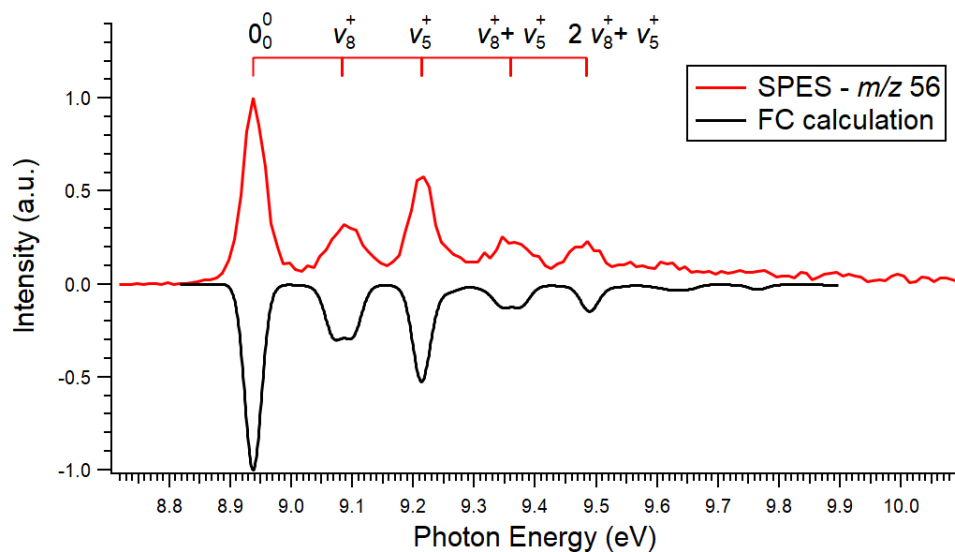
Time-of-flight mass spectrum (TOF-MS) of MKE, its dimer, and its trimer, photoionized at $h\nu = 12.5$ eV.

336x199mm (72 x 72 DPI)

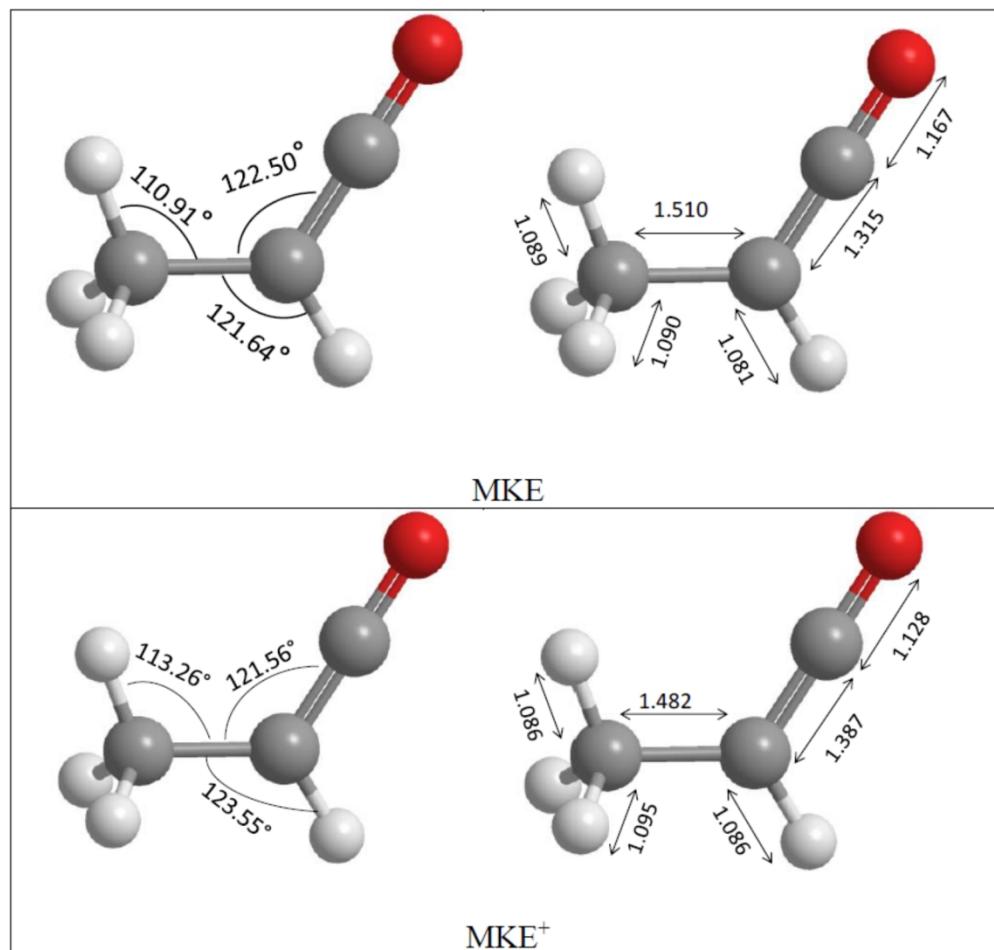


Time-of-flight mass spectrum (TOF-MS) of MKE and the different fragments formed by photoionization at $h\nu = 15.5 \text{ eV}$.

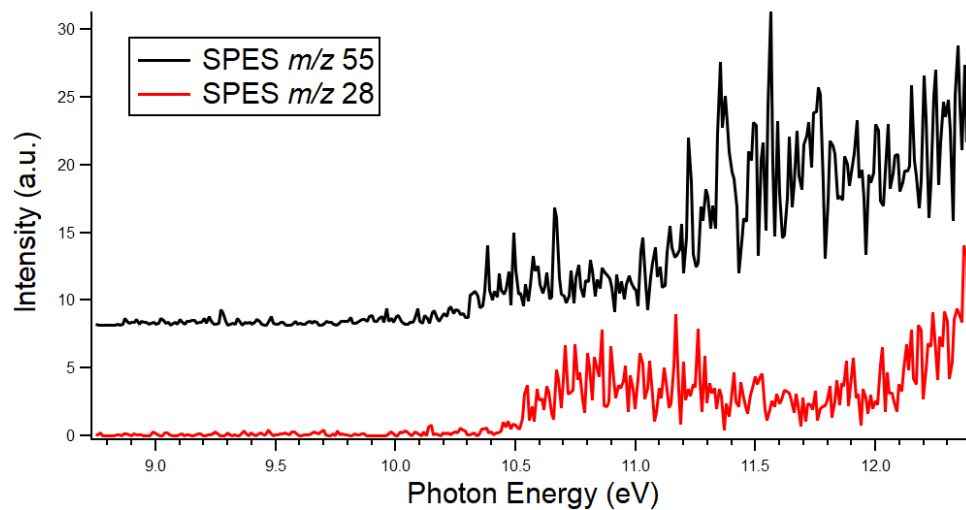
336x199mm (72 x 72 DPI)



Experimental (red) and theoretical (black) SPES of the MKE parent ion (m/z 56). The SPES is obtained by using $eKE_{max} = 100$ meV when diagonally projecting the 2D-PES matrix. The experimental adiabatic ionization energy (AIE) is taken as the median of the 0_0^0 band which is located at 8.937 eV. The assignment of the vibrational progression is discussed in the text. The calculated curve has been shifted upwards in energy by 20 meV to coincide with the experimental results.

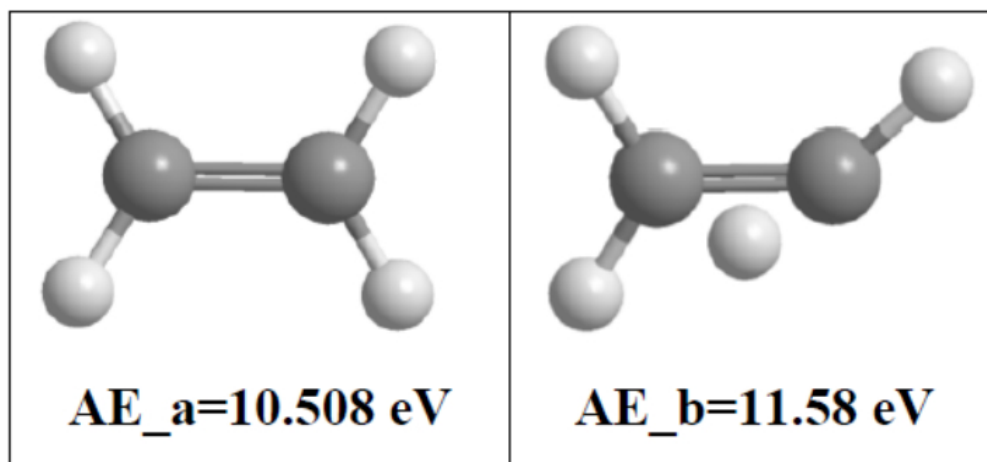


Main geometrical parameters of the ground of neutral MKE and its cation. Distances are given in Å (right panels) and angles are given in degrees (left panels). These geometries are computed at the (R)CCSD(T)-F12 / cc-pVTZ-F12 level.

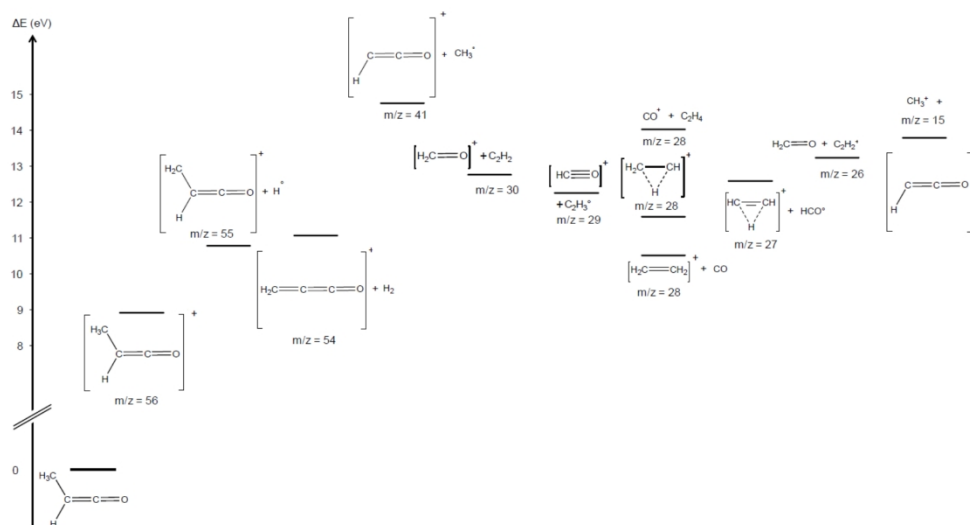


SPES of two fragments formed by dissociative photoionization of MKE. The m/z 55 fragment ion is shown in black and corresponds to H-loss from the parent cation. The m/z 28 fragment ion is shown in red and corresponds to CO loss from the parent cation. In both the m/z 55 and m/z 28 SPES we observed respectively two appearance energies, AE_a and AE_b, for two fragments, a and b, having the same mass. The ranges of the four AEs are indicated as estimated by the experimental accuracy. See text for further details.

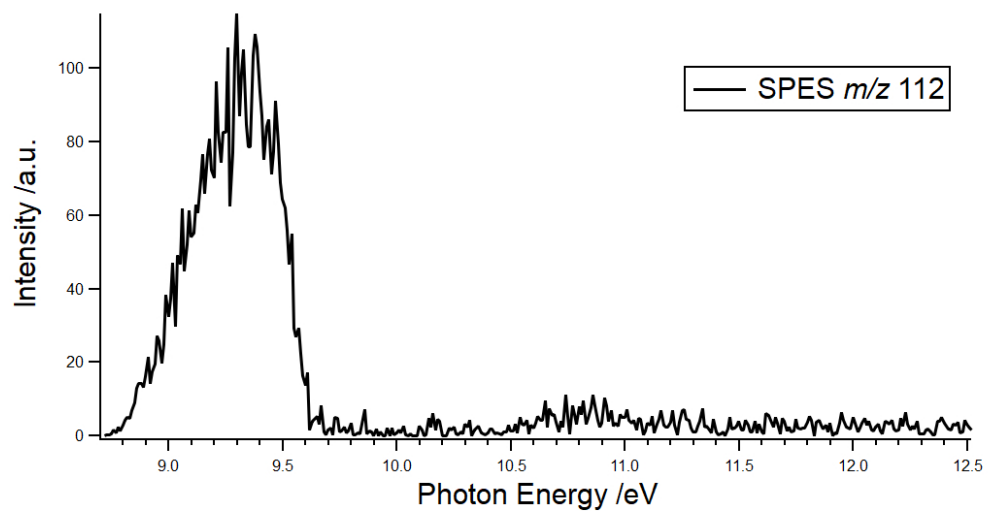
363x188mm (72 x 72 DPI)



Optimized structures of two isomers of C_2H_2^+ calculated at the (R)CCSD(T)-F12 / cc-pVTZ-F12 level. Theoretical AEs are indicated. See text for more details.

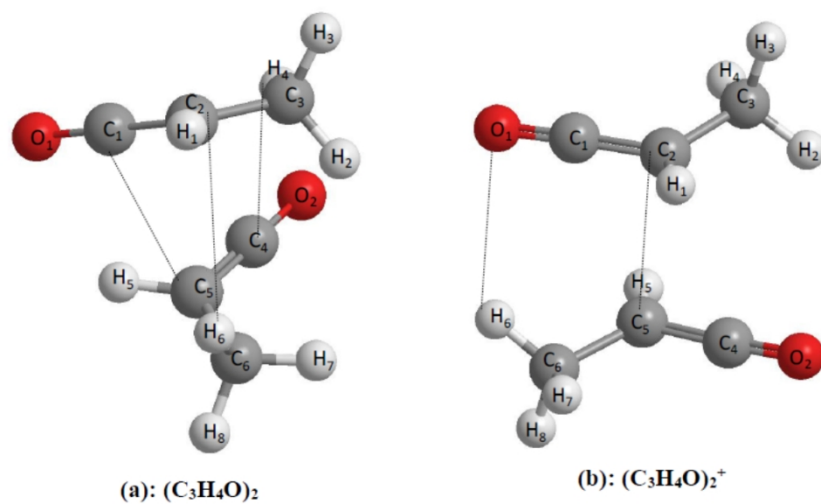


Dissociative ionization fragmentation pathways of the MKE cation considered in the quantum-chemical calculations and relative energies (ordinate) compared to the neutral MKE. The abscissa corresponds to descending m/z values of the formed cationic fragments.

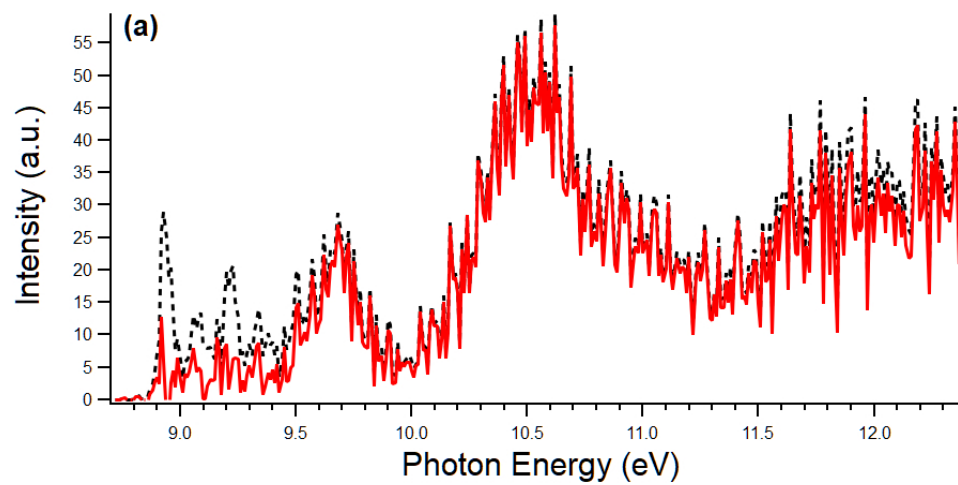


The SPES corresponding to MKE_2 (m/z 112).

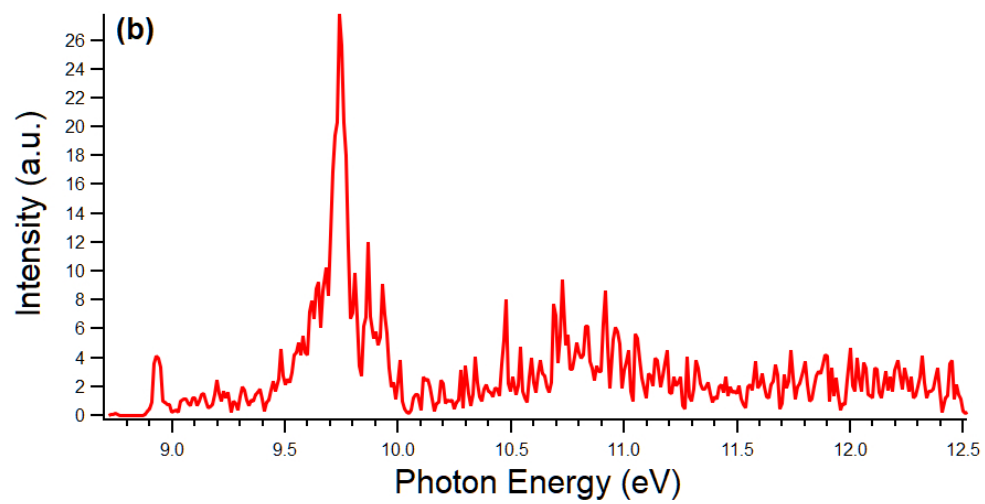
363x187mm (72 x 72 DPI)



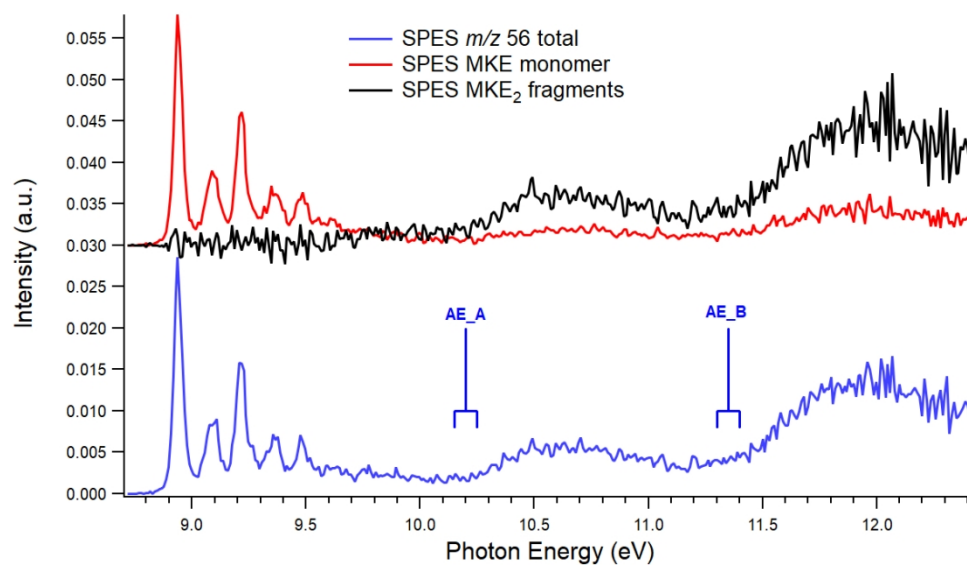
Optimized geometries of MKE₂ (a) and its cation (b).



SPES of the m/z 57 fragment formed by dissociation photoionization of the MKE dimer is presented in red. The m/z 57 signal which includes both the ^{13}C isotopomer signal of the MKE parent and the protonated MKE parent is displayed with the dotted black line.



SPES of the m/z 58 fragment formed by dissociation photoionization of the MKE dimer is presented in red.



Lower panel: SPES of the entire m/z 56 mass peak (cf. Figure 1a; blue line). Upper panel: SPES of the center of the m/z 56 mass peak (red line). Difference spectrum of both treatments (black line). For further explanations, see text. The pattern observed in the lower pattern could correspond to the formation of isomers of the parent ions from the noncovalent dimer (See Table 5). Two onsets (AE_A and AE_B) are indicated.

Supporting Information:

**Unimolecular Decomposition of Methylketene and its Dimer in the Gas
Phase: Theory and Experiment**

Imene Derbali, Helgi Rafn Hrodmarsson, Martin Schwell, Yves Bénilan, Lionel Poisson, Majdi Hochlaf, Mohammad Esmail Alikhani, Jean-Claude Guillemin, Emilie-Laure Zins

Table S1: Optimized geometries of MKE₂ and its cation MKE₂⁺ and there calculated adiabatic ionization energies obtained at the PBE0/aug-cc-pVTZ and at the wB97XD/aug-cc-pVTZ levels of theory.

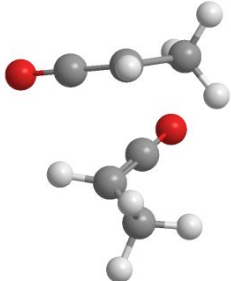
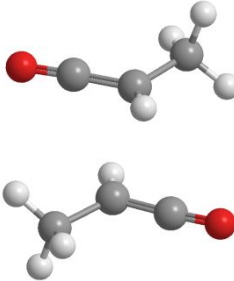
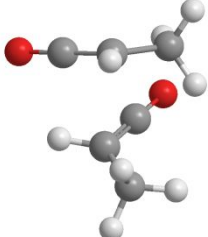
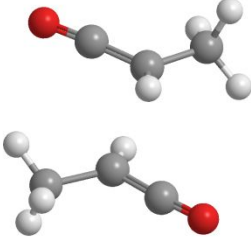
	MKE ₂	MKE ₂ ⁺	Adiabatic ionization energies
PBE0/aug-cc-pVTZ			7.87
wB97XD/aug-cc-pVTZ			7.99

Table S2: Cartesian coordinates of neutral MKE₂, ionized MKE₂⁺ as obtained after geometry optimizations at the PBE0/aug-cc-pVTZ and wB97XD/aug-cc-pVTZ levels of theory.

	MKE ₂				MKE ₂ ⁺			
PBE0/aug-cc-pVTZ	C	1.226164	-1.021245	1.541321	C	0.977419	2.077796	-0.086779
	C	1.379187	-0.885781	0.053309	C	1.021153	0.724703	0.550486
	C	1.956057	0.136636	-0.519617	C	1.821348	-0.254862	0.100618
	O	2.461352	1.052823	-1.025248	O	2.451172	-1.113366	-0.305871
	H	1.690279	-1.942428	1.899641	C	-1.787814	0.252600	-0.214863
	H	0.169945	-1.041700	1.820752	C	-1.009754	-0.806921	-0.483437
	H	1.695335	-0.188396	2.064910	C	-1.047450	-2.059986	0.335140
	H	0.988196	-1.640896	-0.617997	O	-2.405943	1.177502	0.034405
	C	-1.942512	-0.441413	-0.411432	H	1.635218	2.759719	0.460718
	C	-2.060343	0.514606	0.472061	H	-0.030338	2.493163	-0.023109
	C	-1.183228	1.732987	0.504541	H	1.294302	2.057840	-1.127879
	O	-1.846071	-1.294921	-1.193611	H	0.665659	0.575230	1.566211
	H	-2.852930	0.377684	1.198056	H	-1.713330	-2.786879	-0.139565
	H	-1.782238	2.644235	0.447799	H	-0.056538	-2.515626	0.371130
	H	-0.598577	1.773249	1.426966	H	-1.400381	-1.883355	1.349477
	H	-0.484213	1.740302	-0.330349	H	-0.605834	-0.813156	-1.492253
wB97XD/aug-cc-pVTZ	C	1.135395	-0.548302	1.749262	C	0.810539	2.101735	0.004879
	C	1.349763	-0.838812	0.286575	C	0.955940	0.715924	0.566040
	C	2.003009	-0.041472	-0.515089	C	1.841254	-0.163186	0.065375
	O	2.577788	0.674189	-1.225050	O	2.538547	-0.938106	-0.388817
	H	1.524292	-1.357987	2.366655	C	-1.801915	0.155262	-0.255232
	H	0.071651	-0.435004	1.963943	C	-0.919245	-0.836496	-0.457950
	H	1.638947	0.369426	2.048213	C	-0.900762	-2.069501	0.401943
	H	0.943189	-1.732277	-0.166549	O	-2.500392	1.029989	-0.052866
	C	-1.965914	-0.501773	-0.353814	H	1.462064	2.786882	0.549741
	C	-2.071985	0.610651	0.323039	H	-0.211168	2.451937	0.144753
	C	-1.144098	1.784326	0.150224	H	1.064251	2.148081	-1.051178
	O	-1.880192	-1.492262	-0.951858	H	0.639196	0.493495	1.578466
	H	-2.882798	0.644186	1.037588	H	-1.493299	-2.854702	-0.069664
	H	-1.702808	2.685449	-0.102847	H	0.117371	-2.445929	0.492121
	H	-0.589054	1.979377	1.069117	H	-1.301515	-1.883443	1.395056
	H	-0.421209	1.603702	-0.642029	H	-0.497017	-0.853808	-1.456159

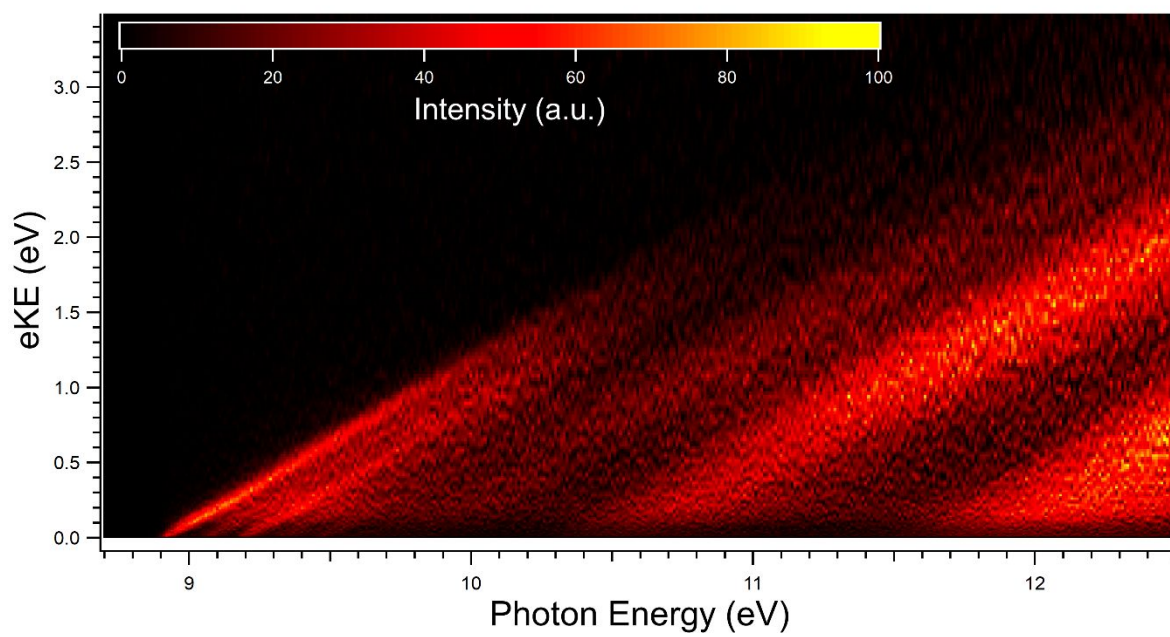


Figure S1. 2D-PES matrix of the m/z 56 mass signals.

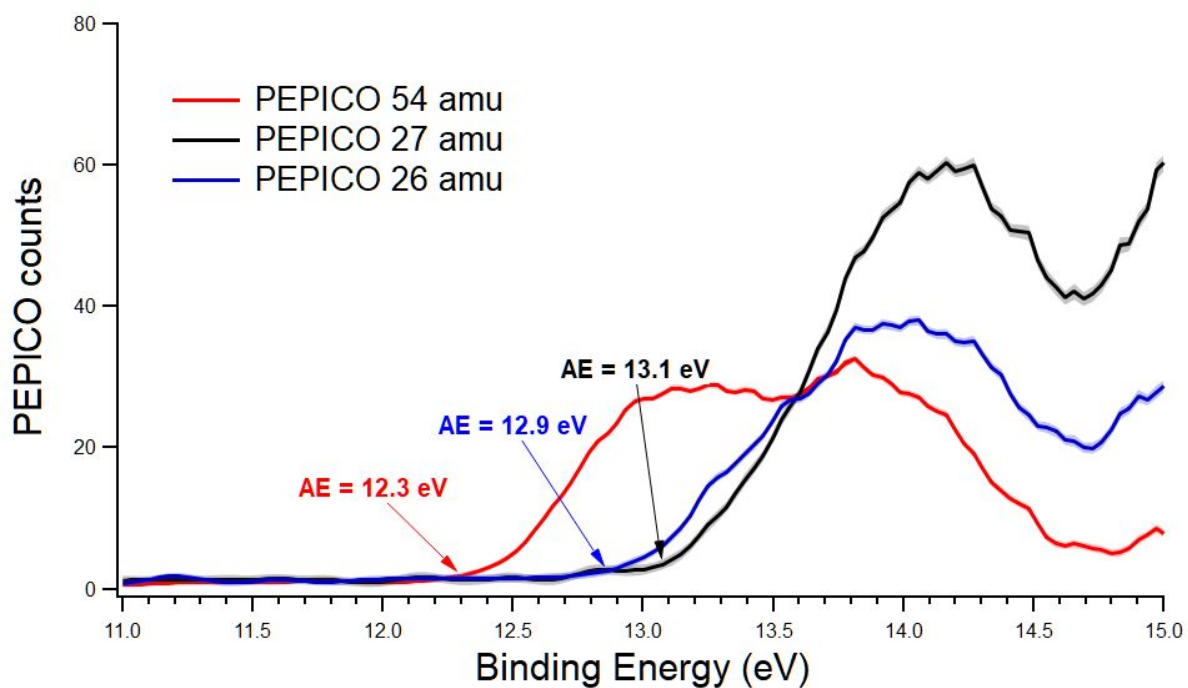


Figure S2. Mass selected PEPICO spectra obtained at 15.5 eV for m/z 54 (red), m/z 27 (black) and m/z 26 (blue). The appearance energies are derived as the first point where the signal increases above the background. This method is less accurate than using recorded SPES and hence we give an estimated error of 0.1 eV for the derived appearance energies.

Table S3: Cartesian coordinates of neutral MKE, ionized MKE and its fragments as obtained after geometry optimizations at the CCSD (T)-F12/cc-pVTZ-F12 level of theory.

C ₃ H ₄ O				C ₃ H ₄ O ⁺			
C	-1.6835996785	-0.3306593240	-0.0000180628	C	-1.6771932832	-0.3442653468	0.0001182243
C	-0.4813060320	0.5822873294	0.0000257105	C	-0.5220531179	0.5837508947	0.0001138047
C	0.7526353148	0.1262125525	-0.0000361211	C	0.7844428304	0.1168639687	-0.0000887145
O	1.8448718328	-0.2845982987	-0.0001070977	O	1.8422077592	-0.2765816933	-0.0002865560
H	-2.3008893352	-0.1618850329	-0.8831006750	H	-2.2949103857	-0.1216438613	-0.8769343890
H	-2.3007023705	-0.1622351975	0.8832630473	H	-2.2939505177	-0.1227565128	0.8781521156
H	-1.3780280750	-1.3763389699	-0.0002606010	H	-1.3866719594	-1.3908983926	-0.0006637606
C ₃ H ₃ O ⁺				C ₂ H ₃ ⁺			
C	-1.3415905194	-0.4160344059	0.4546761816	C	-0.6125918687	-0.0772930734	-0.0000449781
C	-0.3239588476	0.4688524157	0.4505025777	C	0.6126722375	-0.0773587446	-0.0001313718
C	0.9879869372	-0.0417745839	0.4446716469	H	-1.6903309849	-0.0709653605	-0.0005232490
O	2.0333603206	-0.4481189207	0.4390378199	H	1.6904116286	-0.0706727247	0.0002868030
H	-2.3608732403	-0.0518705411	0.4591216137	H	-0.0001340124	1.0473079032	-0.0000032041
H	-1.1778296628	-1.4865868159	0.4529499665				
H	-0.4130949877	1.5485328517	0.4520401936				
C ₃ H ₂ O ⁺				C ₂ H ₄ ⁺ _1			
C	0.5117570972	-0.6259750498	0.0000000000	C	0.7253572054	-0.1328836903	-0.0942607431
C	0.0021893679	0.6681399976	0.0000000000	C	-0.6153527566	0.0422801726	-0.0589134432
O	-0.2023064021	-1.6349797642	0.0000000000	H	1.6132516684	0.4859531528	-0.0112312927
C	-0.3875368200	1.8169295191	0.0000000000	H	-1.2888589146	-0.8072373213	-0.1677649898
H	1.5977951174	-0.8459258166	0.0000000000	H	0.0587060314	-0.2295186937	1.0330641262
H	-0.7387433603	2.8298761139	0.0000000000	H	-1.0435072340	1.0435123799	0.0504473426
C ₂ OH				C ₂ OH ⁺			
C	-0.9908396727	-0.0548506181	0.0000000000	C	-1.1153716462	-0.1226308642	0.0000000000
C	0.2402905378	-0.4825619496	0.0000000000	C	0.2673755009	-0.4811108247	0.0000000000
O	1.2518511619	-1.0721840225	0.0000000000	O	1.2539508361	-1.0307821896	0.0000000000
H	-1.4113020268	0.9325965901	0.0000000000	H	-1.3159546907	0.9575238785	0.0000000000
HCO ⁺				CH ₂ O ⁺			
C	0.0000000000	0.0000000000	-0.5172798898	C	-0.0000035186	-0.5313459258	-0.0000000002
O	0.0000000000	0.0000000000	0.5905155470	O	0.0000075170	0.6626776664	-0.0000000004
H	0.0000000000	0.0000000000	-1.6108956572	H	-0.0000319992	-1.0779518700	-0.9705085941
				H	-0.0000319992	-1.0779518705	0.9705085942
C ₂ H ₄				C ₂ H ₄ ⁺			
C	0.6668209247	-0.0000184102	0.0002794630	C	0.7012972277	-0.0000206895	0.0001142941

C	-0.6668205986	0.0000274047	0.0002816600	C	-0.7012969173	0.0000258878	0.0001102854
H	1.2309854972	-0.9236495911	0.0005519684	H	1.2540868174	-0.9208237665	-0.1608712191
H	1.2310486376	0.9235742781	0.0005441274	H	1.2540228220	0.9206519565	0.1621335332
H	-1.2309851471	0.9236585929	0.0005803085	H	-1.2540869497	0.9208345838	-0.1608408218
H	-1.2310483137	-0.9235652744	0.0005734728	H	-1.2540220000	-0.9206409720	0.1621649282
CO				CO ⁺			
C	0.0000000000	0.0000000000	-0.6465754168	C	0.0000000000	0.0000000000	-0.6380070863
O	0.0000000000	0.0000000000	0.4840774168	O	0.0000000000	0.0000000000	0.4788530863
C ₂ H ₃				C ₂ H ₂ ⁺			
C	-0.7105978953	-0.1520528045	-0.0001448734	C	0.0000000000	0.0000000000	0.6250554878
C	0.5897028040	0.0273704924	-0.0000676627	C	0.0000000000	0.0000000000	-0.6250554878
H	-1.5921428740	0.4693229862	0.0000263161	H	0.0000000000	0.0000000000	1.7037339807
H	1.0214515636	1.0279432494	0.0000225666	H	0.0000000000	0.0000000000	-1.7037339807
H	1.2842164018	-0.8052729235	0.0000456534				
C ₂ H ₂ ⁺							
C	0.0000000000	0.0000000000	0.6027520933				
C	0.0000000000	0.0000000000	-0.6027520933				
H	0.0000000000	0.0000000000	1.6658833002				
H	0.0000000000	0.0000000000	-1.6658833002				

Table S4: Cartesian coordinates of neutral MKE₂, ionized MKE₂ and its fragments as obtained after geometry optimizations at the PBE0/aug-cc-pVTZ level of theory.

(C ₃ H ₄ O) ₂				(C ₃ H ₄ O) ₂ ⁺			
C	1.226164	-1.021245	1.541321	C	0.977419	2.077796	-0.086779
C	1.379187	-0.885781	0.053309	C	1.021153	0.724703	0.550486
C	1.956057	0.136636	-0.519617	C	1.821348	-0.254862	0.100618
O	2.461352	1.052823	-1.025248	O	2.451172	-1.113366	-0.305871
H	1.690279	-1.942428	1.899641	C	-1.787814	0.252600	-0.214863
H	0.169945	-1.041700	1.820752	C	-1.009754	-0.806921	-0.483437
H	1.695335	-0.188396	2.064910	C	-1.047450	-2.059986	0.335140
H	0.988196	-1.640896	-0.617997	O	-2.405943	1.177502	0.034405
C	-1.942512	-0.441413	-0.411432	H	1.635218	2.759719	0.460718
C	-2.060343	0.514606	0.472061	H	-0.030338	2.493163	-0.023109
C	-1.183228	1.732987	0.504541	H	1.294302	2.057840	-1.127879
O	-1.846071	-1.294921	-1.193611	H	0.665659	0.575230	1.566211
H	-2.852930	0.377684	1.198056	H	-1.713330	-2.786879	-0.139565
H	-1.782238	2.644235	0.447799	H	-0.056538	-2.515626	0.371130
H	-0.598577	1.773249	1.426966	H	-1.400381	-1.883355	1.349477
H	-0.484213	1.740302	-0.330349	H	-0.605834	-0.813156	-1.492253
C ₃ H ₅ O ⁺				C ₃ H ₅ O ⁺ _1			
C	0.797992	0.133284	-0.000011	C	-0.898812	0.798235	0.000000
O	1.817881	-0.313257	0.000005	C	-0.934549	-0.761771	0.000000
C	-0.521914	0.663523	-0.000002	C	0.271325	-0.016567	0.000000
C	-1.581030	-0.460909	-0.000001	O	1.516343	-0.119357	0.000000
H	-0.583664	1.308666	0.888099	H	-1.155901	1.326192	0.916000
H	-0.583680	1.308672	-0.888074	H	-1.155901	1.326192	-0.916000
H	-1.496720	-1.078661	0.891699	H	-1.215462	-1.277818	-0.916000
H	-1.496770	-1.078613	-0.891737	H	-1.216462	-1.277818	0.916000
H	-2.552506	0.030602	0.000058	H	1.985198	0.738722	0.000000
C ₃ H ₅ O ⁺ _2				C ₃ H ₅ O			
C	-1.778340	0.135117	-0.000212	C	-1.867472	-0.161956	0.015726
C	-0.443592	-0.440572	0.000258	C	-0.486950	0.400861	-0.040666
C	0.729027	0.348201	0.000652	C	0.613046	-0.318578	-0.015841
O	1.879659	-0.113156	-0.000377	O	1.887098	0.043628	0.100548
H	-2.333126	-0.255026	-0.866791	H	-2.410638	0.218223	0.885335
H	-1.803254	1.222195	-0.000359	H	-1.844363	-1.249705	0.078969
H	-2.333521	-0.254754	0.866249	H	-2.445245	0.117654	-0.869391
H	-0.301151	-1.517590	0.000132	H	-0.372638	1.483622	-0.121101
H	0.691216	1.453947	-0.000402	H	2.424361	-0.440783	-0.533509
C ₃ H ₃ O ⁺				C ₃ H ₃ O			
C	1.606482	-0.382833	0.000008	C	1.699290	-0.348240	0.000002
C	0.629816	0.540848	-0.000003	C	0.578726	0.498553	0.000004
C	-0.693217	0.114470	0.000049	C	-0.696475	0.106171	0.000001

O	-1.760653	-0.217468	-0.000025	O	-1.808365	-0.222249	-0.000004
H	2.643132	-0.064385	-0.000057	H	2.687230	0.083594	-0.000060
H	1.403453	-1.448006	-0.000018	H	1.596732	-1.422646	0.000031
H	0.780158	1.617230	-0.000049	H	0.693708	1.578147	0.000021
C_3H_6O				$C_3H_6O^+$			
C	-1.881030	0.113698	0.000050	C	1.858067	0.123779	0.000119
C	-0.491300	-0.425176	-0.000070	C	0.509909	-0.415674	-0.000099
C	0.589636	0.341352	-0.000087	C	-0.639603	0.382096	0.000085
O	1.851384	-0.175527	0.000065	O	-1.790249	-0.198645	0.000092
H	-2.440841	-0.220867	0.878470	H	2.408912	-0.279268	0.862976
H	-2.441267	-0.221703	-0.877771	H	1.906747	1.210432	0.000741
H	-1.884942	1.205699	-0.000469	H	2.408484	-0.277785	-0.863805
H	-0.355899	-1.502765	-0.000088	H	0.355103	-1.492168	-0.000463
H	0.518926	1.426584	-0.000087	H	-0.587208	1.469293	-0.000550
H	2.489115	0.538024	0.000068	H	-2.540281	0.417441	-0.000269
C_3H_2O				$C_3H_2O^+$			
C	0.910473	1.581763	0.000000	C	0.498476	-0.621087	0.000000
C	0.000000	0.629043	0.000000	C	0.000000	0.665929	0.000000
C	-0.313538	-0.622530	0.000000	O	-0.195748	-1.640484	0.000000
O	-0.774037	-1.691621	0.000000	C	-0.381378	1.810136	0.000000
H	0.631735	2.632816	0.000000	H	1.590817	-0.832481	0.000000
H	1.978947	1.370499	0.000000	H	-0.727424	2.826482	0.000000
$C_2H_3^+$				$C_2H_2^+$			
C	-0.609103	-0.075078	-0.000001	C	0.000000	0.000000	0.627339
C	0.609114	-0.075097	0.000005	C	0.000000	0.000000	-0.627339
H	-1.688902	-0.075838	-0.000007	H	0.000000	0.000000	1.714910
H	1.688914	-0.075745	-0.000020	H	0.000000	0.000000	-1.714910
H	-0.000078	1.052636	0.000000				

Table S5. Cartesian coordinates of the $C_3H_4O^+$ isomers, other than MKE as obtained after geometry optimizations at the PBE0/aug-cc-pVTZ level of theory.

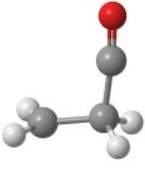
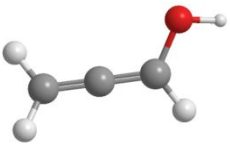
							
$CH_2CH_2CO^+$				$CH_2=C=CHOH^+$			
C	1.519231	-0.525248	-0.000002	C	1.923149	-0.192517	-0.000027
C	0.630976	0.683200	0.000039	C	0.647653	0.164274	-0.010207
C	-0.712120	0.169620	0.000082	C	-0.630969	0.513486	-0.022992
O	-1.709459	-0.330001	-0.000094	O	-1.641188	-0.468243	0.062419
H	1.793271	-0.978910	-0.941473	H	2.701527	0.514552	0.390421
H	1.792279	-0.979593	0.941440	H	2.221900	-1.213532	-0.356764
H	0.730732	1.316554	0.892403	H	-0.911580	1.585274	-0.205512
H	0.730872	1.316525	-0.892335	H	-2.521340	-0.051804	-0.128137

Table S6. Details on the calculations from Table 3 (energies in Hartree). ΔZPE is evaluated at the PBE0/aVTZ level using the corresponding anharmonic frequencies.

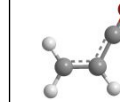
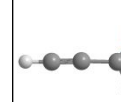
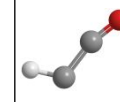
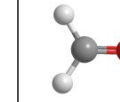
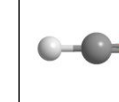
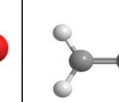
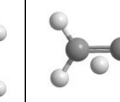
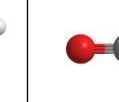
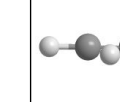
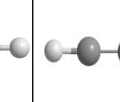
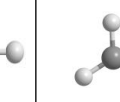
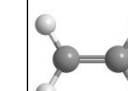
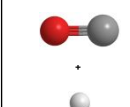
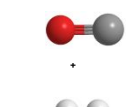
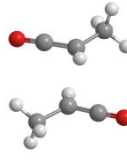
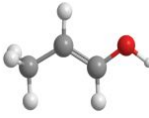
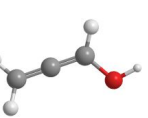
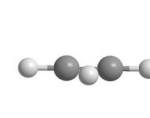
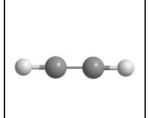
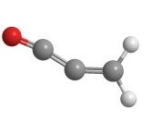
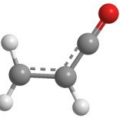
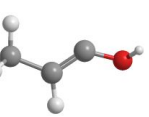
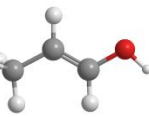
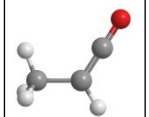
	Neutral	Ionization		Fragments									
	C_3H_4O	$C_3H_4O^{+\circ}$	$C_3H_3O^+$	$C_3H_2O^{+\circ}$	C_2HO^+	$CH_2O^{+\circ}$	HCO^+	$C_2H_4^{+\circ}$	$C_2H_4^{+\circ}_{-1}$	$CO^{+\circ}$	$C_2H_3^+$	$C_2H_2^{+\circ}$	CH_3^+
													
			+ H	H ₂	CH ₃	C ₂ H ₂	C ₂ H ₃	+ CO	+ CO	C ₂ H ₄	H+CO	H ₂ +CO	C ₂ HO
													
	MKE	m/z = 56	m/z = 55	m/z = 54	m/z = 41	m/z = 30	m/z = 29	m/z = 28	m/z = 28	m/z = 28	m/z = 27	m/z = 26	m/z = 15
$E_{\text{corr}}^{(R)} = E_{\text{F12/cc-pVTZ-F12}}^{(R)} - E_{\text{F12/cc-pVTZ-F12}}^{(R)}_{\text{CCSD(T)}}$	-191.6727871	-191.3444769	-190.76708	-190.0170729	-151.34361	-113.978169	-113.434236	-78.08131501	-78.0383262	-112.684811	-77.46773556	-76.7976175	-39.4166771
$\Delta ZPVE$	0.061127	0.060027	0.05086	0.035518	0.018075	0.024017	0.016532	0.048681	0.045396	0.005307	0.034511	0.026117	0.031245
ΔCV	-0.19848764	-0.1980106	-0.19794229	-0.19788533	-0.14831673	-0.10090312	-0.1009479	-0.09619585	-0.09632495	-0.10023646	-0.09667361	-0.09612749	-0.04761424
ΔSR	0.00689882	0.00689129	0.00689727	0.00696941	0.00612191	0.0053068	0.00530276	0.0016243	0.00162836	0.00538693	0.00164178	0.0016518	0.00081066
$E_{\text{corr}} = E_{\text{F12}}^{(R)} + \Delta CV + \Delta SR + \Delta ZPE$	-191.8032489	-191.4755692	-190.907265	-190.1724708	-151.4677298	-114.049748	-113.513349	-78.12720556	-78.0876268	-112.774353	-77.52825639	-76.8659762	-39.4322357

Table S7. Details on the calculations from Table 4 (energies in Hartree). ΔZPE is evaluated at the PBE0/aVTZ level.

	Neutral	Ionization	Fragments									
	$(C_3H_4O)_2$	$(C_3H_4O)_2^{+\bullet}$	$C_3H_6O^{+\bullet}$	$C_3H_5O^+$	$C_3H_5O^+_1$	$C_3H_5O^+_2$	$C_3H_4O^{\bullet}$	$C_3H_4O^+_1$	$C_3H_3O^+$	$C_3H_2O^+$	$C_2H_3^+$	$C_2H_2^+$
												
			C_3H_2O	C_3H_3O	C_3H_3O	C_3H_3O	C_3H_4O	C_3H_4O	C_3H_5O	C_3H_6O	C_3H_6O	C_3H_4O
												
											+CO	+HCO
	MKE_2	$m/Z = 112$	$m/Z = 58$	$m/Z = 57$	$m/Z = 57$	$m/Z = 57$	$m/Z = 56$	$m/Z = 56$	$m/Z = 55$	$m/Z = 54$	$m/Z = 27$	$m/Z = 26$
PBE0/aug-cc-pVTZ	-383.41329	-383.124181	-192.590662	-192.021935	-191.973235	-191.923076	-191.362476	-191.31812	-190.805736	-190.075952	-77.477487	-76.818604

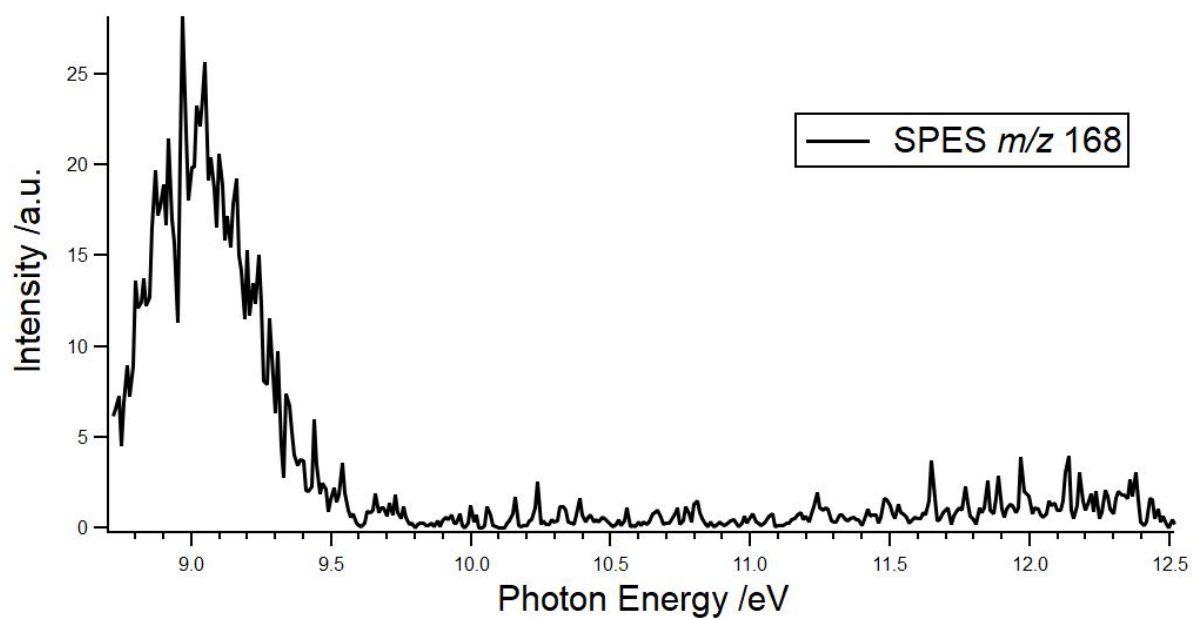


Figure S3. The SPES corresponding to the MKE trimer (m/z 168).

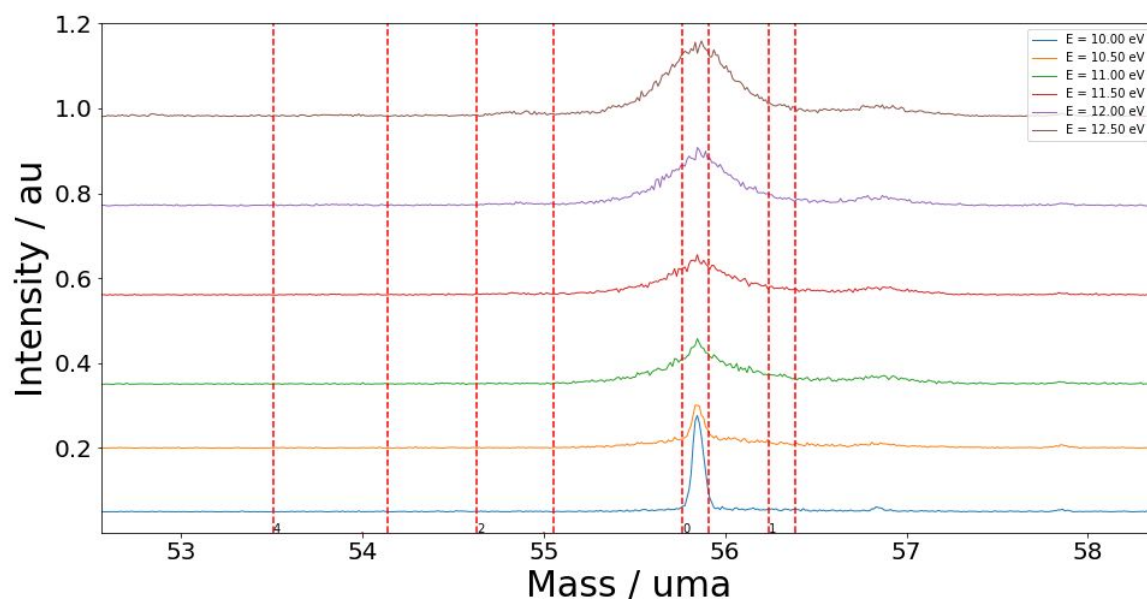


Figure S4. Peak evolution of the m/z 56 signal with increasing photon energy.

Table S8. Attribution of excited states of the MKE cation (m/z 56) calculated at the MRCI/aVTZ level of theory (in eV).

Ground State	8.917
1 st excited state	13.51
2 nd excited state	14.21

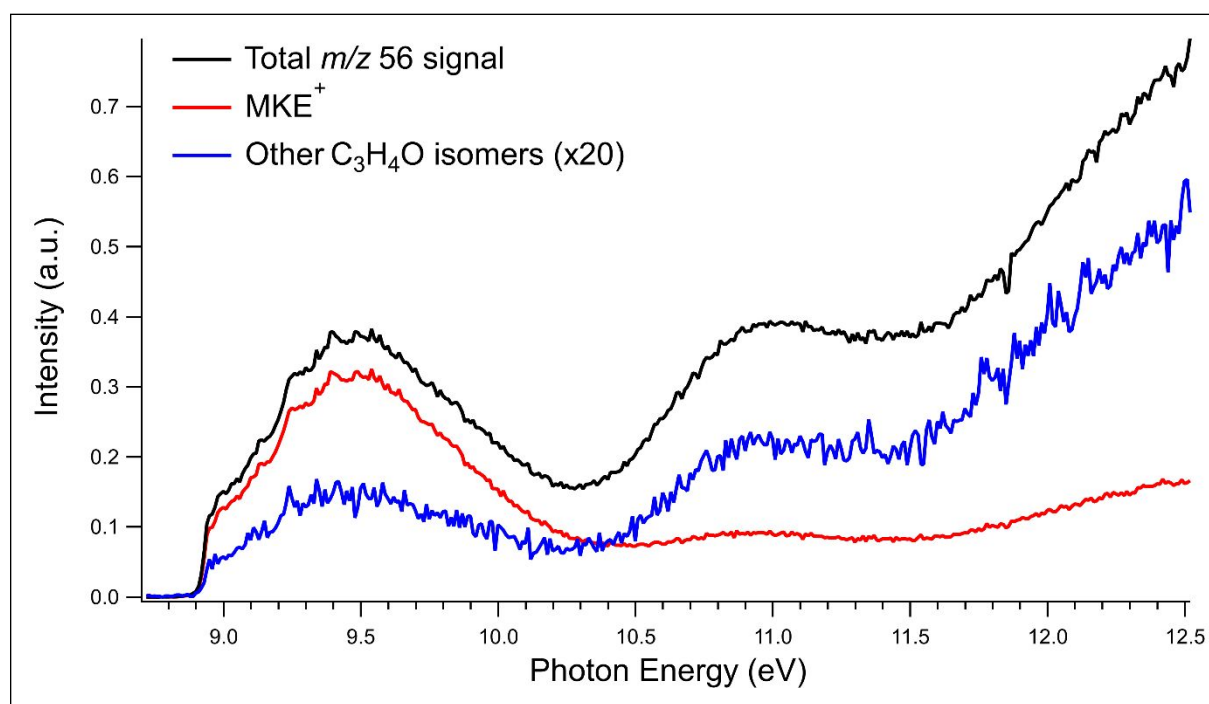
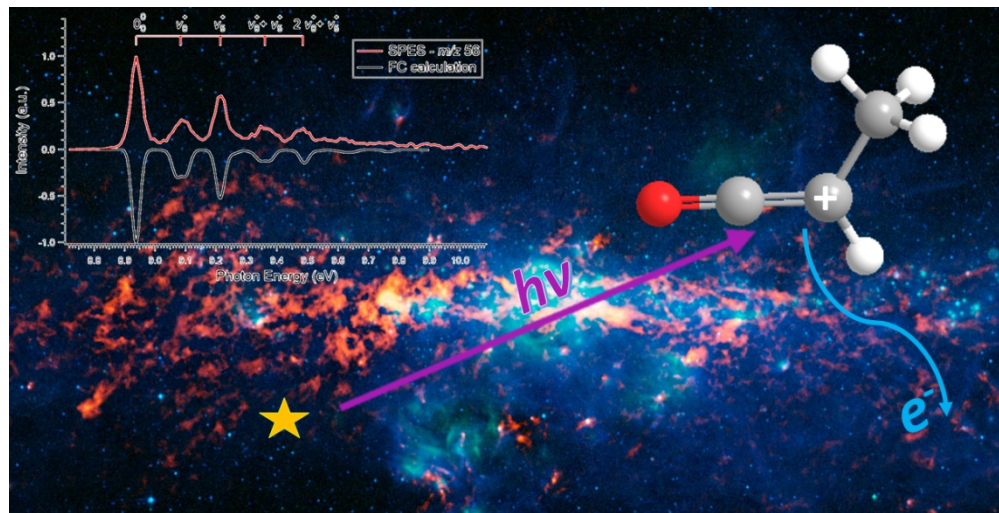
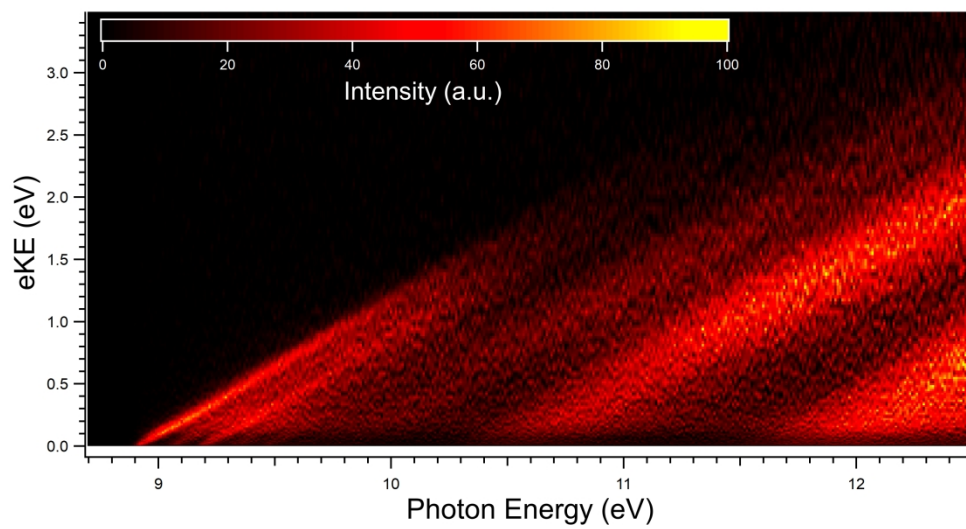
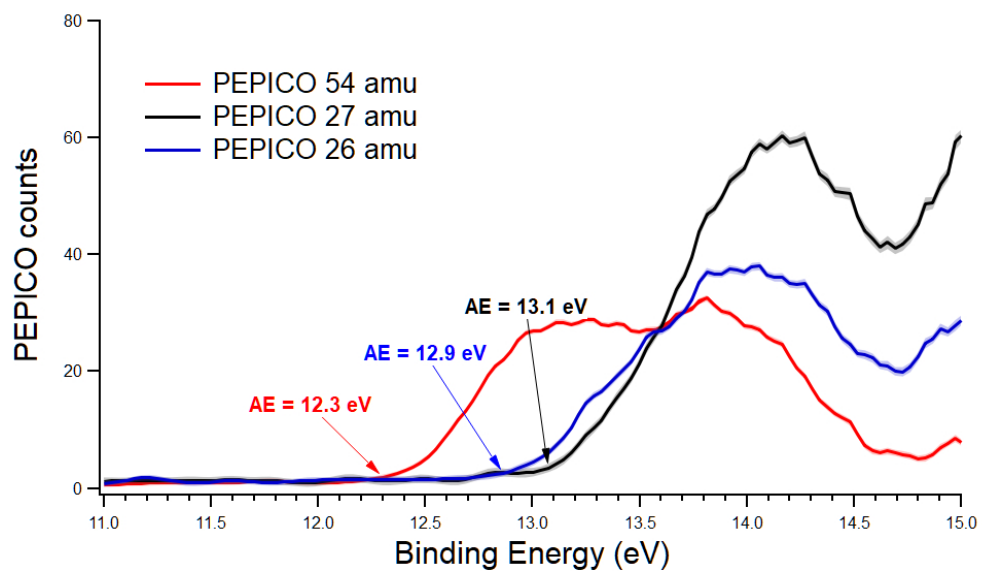


Figure S5. Total ion yield (TIY) of the m/z 56 signal (black). By employing the same filtering as was done on the m/z 56 SPES the signal can be disentangled into the contribution of the ionized MKE monomer (red) and that of the C₃H₄O⁺ fragments formed by dissociative ionization of the MKE dimer.

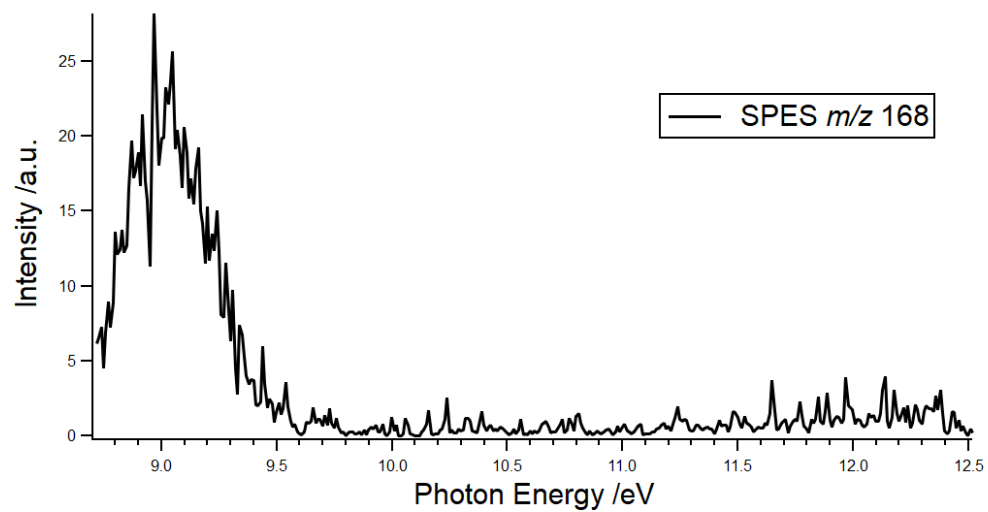




2D-PES matrix of the m/z 56 mass signals.

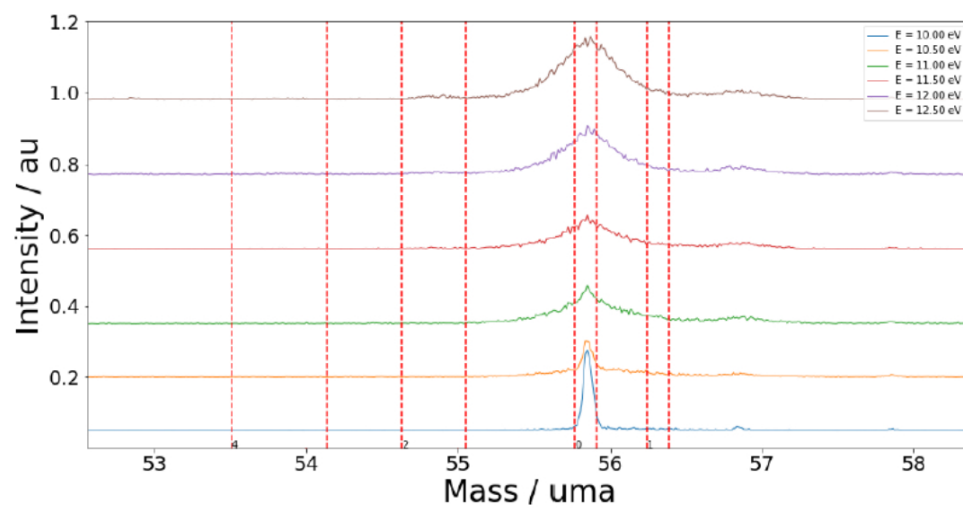


Mass selected PEPICO spectra obtained at 15.5 eV for m/z 54 (red), m/z 27 (black) and m/z 26 (blue). The appearance energies are derived as the first point where the signal increases above the background. This method is less accurate than using recorded SPES and hence we give an estimated error of 0.1 eV for the derived appearance energies.

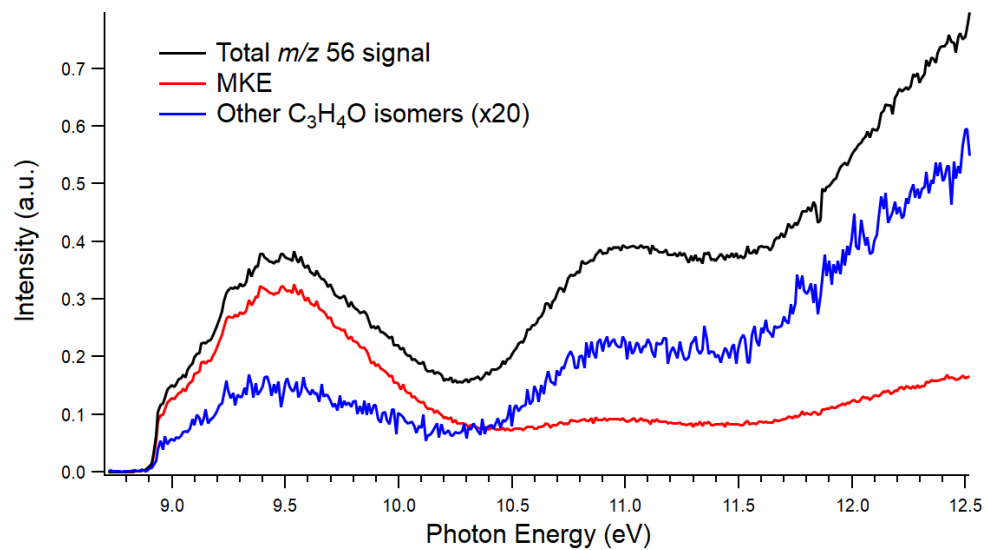


The SPES corresponding to the MKE trimer (m/z 168).

363x187mm (72 x 72 DPI)



Peak evolution of the m/z 56 signal with increasing photon energy.



Total ion yield (TIY) of the m/z 56 signal (black). By employing the same filtering as was done on the m/z 56 SPES the signal can be disentangled into the contribution of the ionized MKE monomer (red) and that of the $C_3H_3O^+$ fragments formed by dissociative ionization of the MKE dimer.

406x226mm (72 x 72 DPI)